International Journal of Nanomedicine

Dovepress
open access to scientific and medical research

Open Access Full Text Article

ORIGINAL RESEARCH

Tumor Cell-Targeting and Tumor Microenvironment–Responsive Nanoplatforms for the Multimodal Imaging-Guided Photodynamic/Photothermal/Chemodynamic Treatment of Cervical Cancer

Ying Wang[1,*], Yiyan Xu[2,*], Jiayu Song[1], Xueting Liu[1], Sijia Liu[1], Nan Yang[1], Le Wang[1], Yujie Liu[1], Yiwei Zhao[1], Wenhu Zhou[3,4], Yunyan Zhang[1]

[1]Department of Gynecological Radiotherapy, Harbin Medical University Cancer Hospital, Harbin, Heilongjiang, 150081, People's Republic of China; [2]Department of Vascular Surgery, The First Affiliated Hospital of Guangzhou Medical University, Guangzhou, Guangdong, 510120, People's Republic of China; [3]Xiangya School of Pharmaceutical Sciences, Central South University, Changsha, Hunan, 410013, People's Republic of China; [4]Hunan Key Laboratory of The Research and Development of Novel Pharmaceutical Preparations, School of Pharmaceutical Science, Changsha Medical University, Changsha, 410219, People's Republic of China

*These authors contributed equally to this work

Correspondence: Yunyan Zhang, Department of Gynecological Radiotherapy, Harbin Medical University Cancer Hospital, No. 150, Haping Road, Nangang District, Harbin, Heilongjiang Province, 150081, People's Republic of China, Tel +86 13604843878, Fax +86 451 85718392, Email zhangyunyan@hrbmu.edu.cn; Wenhu Zhou, Xiangya School of Pharmaceutical Sciences, Central South University, 172 Tongzipo Road, Changsha, Hunan, 410013, People's Republic of China, Tel +86 15111469284, Fax +86 731 88710591, Email zhouwenhuyaoji@163.com

Purpose: Phototherapy, known for its high selectivity, few side effects, strong controllability, and synergistic enhancement of combined treatments, is widely used in treating diseases like cervical cancer.

Methods: In this study, hollow mesoporous manganese dioxide was used as a carrier to construct positively charged, poly(allylamine hydrochloride)–modified nanoparticles (NPs). The NP was efficiently loaded with the photosensitizer indocyanine green (ICG) via the addition of hydrogen phosphate ions to produce a counterion aggregation effect. HeLa cell membrane encapsulation was performed to achieve the final M-HMnO_2@ICG NP. In this structure, the HMnO_2 carrier responsively degrades to release ICG in the tumor microenvironment, self-generates O_2 for sensitization to ICG-mediated photodynamic therapy (PDT), and consumes GSH to expand the oxidative stress therapeutic effect [chemodynamic therapy (CDT) + PDT]. The ICG accumulated in tumor tissues exerts a synergistic PDT/photothermal therapy (PTT) effect through single laser irradiation, improving efficiency and reducing side effects. The cell membrane encapsulation increases nanomedicine accumulation in tumor tissues and confers an immune evasion ability. In addition, high local temperatures induced by PTT can enhance CDT. These properties of the NP enable full achievement of PTT/PDT/CDT and targeted effects.

Results: Mn^{2+} can serve as a magnetic resonance imaging agent to guide therapy, and ICG can be used for photothermal and fluorescence imaging. After its intravenous injection, M-HMnO_2@ICG accumulated effectively at mouse tumor sites; the optimal timing of in-vivo laser treatment could be verified by near-infrared fluorescence, magnetic resonance, and photothermal imaging. The M-HMnO_2@ICG NPs had the best antitumor effects among treatment groups under near-infrared light conditions, and showed good biocompatibility.

Conclusion: In this study, we designed a nano-biomimetic delivery system that improves hypoxia, responds to the tumor microenvironment, and efficiently loads ICG. It provides a new economical and convenient strategy for synergistic phototherapy and CDT for cervical cancer.

Keywords: phototherapy, reactive oxygen species, hypoxia relief, collaborative therapy

Received: 28 February 2024
Accepted: 23 May 2024
Published: 13 June 2024

Introduction

Cervical cancer is the fourth most common gynecological malignancy in the world, causing more than 300,000 deaths annually.[1] Currently, its clinical treatment relies on surgery.[2] For young patients with reproductive needs, however, this approach is unsatisfactory, as cervical conization increases the risk of miscarriage due to cervical insufficiency and radical surgery renders women infertile.[3,4] Chemotherapy is a necessary adjuvant treatment for cervical cancer, but it has poor efficacy due to treatment tolerance and severe toxic side effects.[5] Thus, the development of new therapeutic strategies for cervical cancer is of great clinical importance.

Given that the cervical anatomical structure is connected to that of the vagina, the use of optical therapies for cervical cancer have attracted extensive research attention.[6,7] Phototherapy, or the administration of photothermal therapy (PTT) and photodynamic therapy (PDT) via near-infrared (NIR) light exposure using photosensitizers (PSs) and photothermal agents, has been used widely in antitumor research.[8–10] As a local treatment method, it has the advantages of non–direct invasiveness, low drug resistance, real-time diagnosis, and good tissue selectivity; it enables photosensitive and photothermal material accumulation at irradiation sites without damaging surrounding normal tissues.[11–13] In PTT, a photothermal reagent converts absorbed NIR light energy into effective thermal energy for the killing of tumor cells through thermal ablation.[14,15] In PDT, PSs convert surrounding molecular O_2 into cytotoxic reactive oxygen species (ROS) under laser irradiation at specific wavelengths to drive cell death.[16–18] PTT and PDT have synergistic effects.[19,20] On one hand, increased hypoxia and acidification of the tumor microenvironment after PDT increase the sensitivity of tumor cells to PTT, and reduced blood flow to the tumor reduces the "heat sink" effect, which aids the achievement of the photocoagulation temperature. On the other hand, the heat generated by PTT increases blood flow, improves the O_2 supply, and significantly enhances PDT-induced injury.[21] Just as laser irradiation with a single light source can facilitate clinical operations, the synergistic use of PDT and PTT against cervical cancer with a single light source is potentially translatable to the clinical setting.

With advances in the field of phototherapy, agents such as protoporphyrin IX, dihydrochlorin e6, and methylene blue (MB) have been approved for the clinical treatment of skin, esophageal, and lung tumors.[9,22] However, the absorption spectra of these PSs fall primarily within the visible light range (<700 nm), and high degrees of light absorption and scattering by biological tissues significantly diminish their effectiveness in deep tissue treatment. NIR light, which falls within the biological transparency window of 700–1000 nm, exhibits deeper tissue penetration and lower absorption rates.[23–25] Thus, the use of PSs with longer wavelength absorption characteristics to enhance phototherapeutic effects warrants consideration.

Indocyanine green (ICG) has a strong absorption peak between 780 and 800 nm, and thus good absorption capacity in the NIR.[26] Due to its low toxicity, high affinity, and unique optical properties, ICG has been approved by the US Food and Drug Administration for clinical application as a NIR organic dye with photothermal and photodynamic capabilities under single-light-source irradiation.[27–30] However, the practical application of ICG entails several challenges related to its propensity for photobleaching, low photothermal conversion efficiency, and poor photostability.[31–34] For instance, under NIR laser exposure, the quantum yield of singlet oxygen ($^1O_2$) generated by ICG monomers is only 0.2%.[23] Furthermore, intravenously injected ICG binds readily to plasma proteins, such as albumin and high-density (eg, α-1) lipoproteins, leading to its rapid clearance from the body and a half-life of only about 2–4 min.[35,36] ICG also lacks specificity, limiting its accumulation in tumor tissues and thereby its application in tumor phototherapy.[37,38] Thus, the development of new nanomedicines to address these issues, enhancing ICG's stability, retention time in the body, and therapeutic effects against tumors, is urgently needed.

Recent advances in nanotechnology have made the combined use of nanomaterials and phototherapy techniques a viable approach for tumor treatment. To improve the therapeutic advantages of ICG and the effect of combined PTT/PDT, researchers have constructed novel composite materials. Xue et al[34] grafted ICG onto nanocarriers with magnetic (Fe_3O_4) nanoparticle cores and Prussian blue nanoshells (formed in situ) using polyethylenimine modification and electrostatic adsorption to improve drug-carrying efficiency and stability, which are conducive to ICG accumulation in tumors. This approach effectively solved the problems of free ICG molecules' poor optical stability and low bioavailability. Chen et al[39] developed a Pd1.7 Bi@CeO_2–ICGcore–shell structure with dual enzyme activity, and reported that the ICG-loaded Pd1.7Bi@CeO_2 exhibited peroxidase- and catalase (CAT)-like activities and synergistic photothermal/photokinetic/chemo-kinetic antitumor efficacy. Its CAT-like activity resulted in in-situ O_2 generation, which alleviated tumor hypoxia and improved the PDT efficiency of the coupled ICG. Cheng et al[40] prepared a nanoscale Cu/Zn metal organic framework (MOF) by introducing Cu^{2+} ions into the precursor of ZIF-90 and explored the formation of mixed-valence ($Cu^{+/2+}$) hollow

porous structures upon heating and mixed-metal, mixed-valence ($Cu^{+/2+}$/$Mn^{2+/4+}$) structures upon heating with the addition of manganese acetylacetonate [$Mn(acac)_2$]. They loaded the hollow structure with ICG (ICG@Mn/Cu/Zn-MOF@MnO_2) for multimodal imaging-guided PTT/PDT/chemodynamic therapy (CDT). These studies have shown that the optical stability of ICG can be improved effectively by encapsulation in nanocarriers, enabling full leveraging of this dye's dual therapeutic advantages and improving its antitumor efficacy. The structural complexity of these multifunctional nanomedicines, however, increases the difficulty of their clinical translation. Thus, the simplification of drug carrier structures, enhancement of drug delivery efficiency, and full leveraging of combined therapeutic effects continue to be challenges.

In this study, we used hollow mesoporous manganese dioxide ($HMnO_2$), which has a high specific surface area and good tumor microenvironment responsiveness, as a carrier. It was modified using poly (allylamine hydrochloride) (PAH) to exploit its cationic properties for reversing the charge of manganese dioxide, thereby overcoming the electrostatic repulsion with the negatively charged ICG molecules. Additionally, hydrogen phosphate ions were added to create a counterion cohesion effect, stabilizing the surface charge state of the material, enhancing adsorption sites, and significantly enhancing the adsorption and encapsulation of ICG molecules.[35,36,41] With this design, efforts were made to enhance the stability of ICG and utilize the CAT-like activity of the carrier to decompose high concentrations of H_2O_2 in tumors into O_2, sensitizing the PDT effect of ICG under laser irradiation. Additionally, with the integration of PTT, the chemodynamic properties of the carrier were enhanced to amplify oxidative stress. The coating of the NP surfaces with HeLa cell membranes enabled the NPs to achieve immune evasion and target homologous tumors. An integrated NP platform was constructed to synergize the effects of PDT/PTT/CDT and exert multimodal imaging functions (Scheme 1).

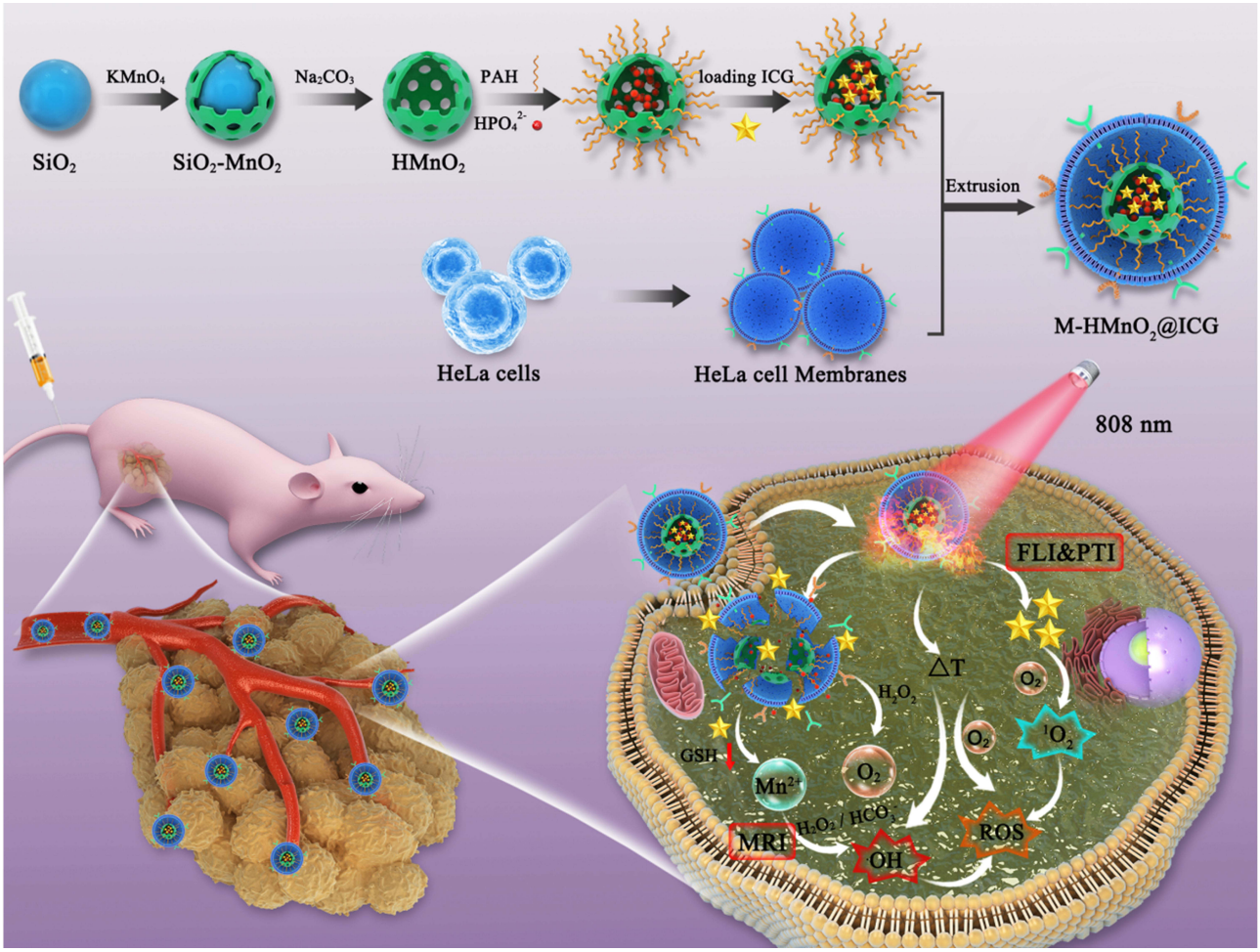

Scheme 1 Schematic diagram of M-$HMnO_2$@ICG preparation and multimodal imaging-guided PTT/PDT/CDT.

An in-vivo mouse model confirmed that M-HMnO$_2$@ICG exerts optimal antitumor treatment effects under NIR irradiation This simplified, cost-effective, tumor microenvironment–responsive integrated nanoplatform thus provides a basis for clinical translation.

Materials and Methods

Materials

Tetraethyl orthosilicate (TEOS), PAH (molecular weight ≈15,000), potassium permanganate, sodium carbonate, and ammonia ($NH_3 \cdot H_2O$) were purchased from Innochem. ICG was purchased from ARK Pharmaceuticals. Hoechst 33,342, phenylmethylsulfonyl fluoride (PMSF), cell counting kit 8 (CCK8), and bicinchoninic acid (BCA) protein assay kits were purchased from Biosharp. Cytoplasmic protein extraction and live-staining dead-dye kits were purchased from Beyotime Biotechnology. All cell culture reagents were purchased from Procell. Deionized water was prepared using a Milli-Q system (Millipore, USA).

HMnO$_2$@ICG Preparation

First, solid SiO_2 NPs were synthesized using a previously reported method.[42] They were washed three times with water and ethanol and then stored in water until use. To synthesize SiO_2@MnO_2 NPs, 300 mg $KMnO_4$ dispersed in 10 mL water was added dropwise to the NPs, followed by 1 h ultrasound treatment and then stirring overnight at room temperature. The obtained SiO_2@MnO_2 NPs were washed three times with deionized water and centrifuged at 12,000 rpm, then dissolved in a Na_2CO_3 solution at 60°C for 12 h to obtain $HMnO_2$ NPs. For ICG loading, these NPs (10 mg) were added to a solution containing 10 mL PAH (5 mg/mL), followed by stirring for 2 h, centrifuging at 12,000 rpm, and washing with water. Phosphate buffer (PB; 20 mM) was added to the obtained H-MnO_2/PAH solution, followed by the addition of ICG in PB (0.3 mg/mL), mixing, and stirring in the dark for 2 h. ICG was then loaded into the solution with centrifuging at 12,000 rpm for 10 min. The resulting HMnO$_2$@ICG mixture was washed three times with deionized water. To further investigate the effects of the loading condition on the drug encapsulation and loading rates, we used $HMnO_2$, $HMnO_2$/PAH, and $HMnO_2$/PAH/HPO_4^{2-} solutions as carriers. We added an aqueous ICG solution with the same content and stirring under the same conditions at a feeding ratio of 2:1, then collected and centrifuged the supernatant. According to the reported standard curve method,[43] the ICG content of the supernatant was measured using an ultraviolet/visible-near infrared (UV/Vis-NIR) spectrophotometer (UV-2600; Shimadzu Corporation, Japan) under $HMnO_2$, $HMnO_2$/PAH, and $HMnO_2$/PAH/HPO_4^{2-} addition conditions. The ICG loading capacity (LC) and encapsulation efficiency (EE) of the NPs were calculated using the following equations:

$$\mathrm{LC}\ (\%) = \frac{\text{weight of loaded ICG}}{\text{total weight NP}} \times 100\%$$

$$\mathrm{EE}(\%) = \frac{\text{weight of loaded ICG}}{\text{total weight ICG}} \times 100\%$$

M-HMnO$_2$@ICG Preparation

To obtain HeLa cell membrane vesicles, human cervical cancer cells were centrifuged for 5 min (1500 rpm, 4°C) and the pure sediment was collected and resuspended in hypotonic lysis buffer containing membrane protein extraction reagent and PMSF. After 1 h incubation in an ice bath, the HeLa cells were transferred to a glass homogenizer for 40 mechanical disruptions, and the resulting mixture was centrifuged (700 × *g*, 10 min, 4°C). The resulting supernatant was centrifuged again at 14,000 × *g* for 30 min. The HeLa cell membrane fragments were collected, freeze dried, quantified, and stored at –20°C. These fragments (1 mg) were redispersed in 1× phosphate-buffered saline (PBS), sonicated for 10s, and then extruded through 800- and 400-nm porous polycarbonate membranes at least 11 times using a LiposoFast extruder (Avestin) to obtain HeLa cell membrane vesicles. The HMnO$_2$@ICG mixture (1 mg/mL, 0.5 mL) was added to these vesicles (2 mg/mL, 0.5 mL), followed by mixing in an ice bath, sonication for 20s, and extrusion through a 400-nm

polycarbonate membrane at least 5 times. The mixture was then centrifuged (5000 × *g*, 30 min, 4°C) and the supernatant was discarded to obtain the final M-HMnO$_2$@ICG formulation.

Material Characterization

The NP morphology, size, and elemental distribution were observed under a transmission electron microscope (TEM; Tecnai G2 F20; FEI, USA). The materials' Brunauer, Emmett, and Teller (BET) surface area and pore volume were determined using an ASAP2460 3.01 nitrogen adsorption-desorption isotherm (Micromeritics, USA). The particles' dynamic light scattering (DLS) and zeta potentials were determined using a Zetasizer Nano ZS90 device (Malvern). X-ray photoelectron spectra collected using an ESCALAB 250Xi microprobe (Thermo Scientific) were used to analyze the NPs' elemental composition and valence distributions. Inductively coupled plasma optical emission spectrometry (ICP-OES) was used to determine the Mn content. Fluorescence spectra were obtained using an F-2700 spectrometer (Hitachi, Japan). UV/Vis-NIR absorption spectra were measured using a UV-2600 spectrometer (Shimadzu, Japan).

Membrane Protein Characterization

The types and contents of membrane proteins in the HMnO$_2$@ICG NPs, HeLa cell membranes, and M-HMnO$_2$@ICG NPs were investigated by sodium dodecyl sulfate polyacrylamide gel electrophoresis (SDS-PAGE). Total proteins were extracted from cell membranes using RIPA lysis buffer, analyzed by electrophoresis, and stained with Komas blue. Western blotting was used to identify surface proteins in the HeLa cell membranes. The Hela cells, HeLa cell membranes, and M-HMnO$_2$@ICG NPs were lysed using RIPA buffer containing PMSF in an ice bath for 30 min and quantified using a BCA kit. These collected proteins were mixed with up-sampling buffer, denatured by boiling in water for 10 min, and subjected to SDS-PAGE (Mini-Protean; Bio-Rad, USA). The gels were then transferred to a polyvinylidene fluoride membrane, sealed with 5% milk in an ice bath for about 1 h, and incubated overnight at 4°C with a monoantibody containing CD47, CD44, E-cadherin, and galactin-3, followed by incubation with the corresponding secondary antibody. Finally, protein signals were observed using a gel imaging system (ChemiDoc XRS; Bio-Rad).

In-Vitro Photothermal Performance Assessment

Aqueous M-HMnO$_2$@ICG solutions (50, 100, 150, and 200 μg/mL, 0.5 mL) were added to centrifuge tubes and irradiated for 6 min using a 1.35-W/cm^2 power density laser, with the real-time monitoring of temperature changes using an NIR thermal imager (FLIR Systems AB). Temperatures were recorded by direct photography with an infrared thermal imager at 0, 1, 3, and 5 min after irradiation. In addition, the temperature changes of an M-HMnO$_2$@ICG aqueous solution (200 μg/mL) irradiated with different laser power densities (0.5, 1.0, and 1.5 W/cm^2) were investigated using the same method. To investigate the photothermal stability of M-HMnO$_2$@ICG, four consecutive heating–cooling cycles were performed. The aqueous M-HMnO$_2$@ICG solution (150 μg/mL, 1 mL) was irradiated for 10 min (808 nm, 1.35 W/cm^2) and then allowed to cool naturally for 11 min. According to the temperature changes that occurred during the cooling stage, its photothermal conversion efficiency (η) was calculated as follows:[44,45]

$$\eta = \frac{hA(\mathrm{T}_{max} - T_{sur}) - Qs}{I\left(1 - 10^{-A_\lambda}\right)}$$

where η is the heat transfer coefficient, A is the surface area of the vessel, $T_{\max}$ is the maximum temperature of the M-HMnO$_2$@ICG aqueous dispersion, T_{sur} is the temperature of the surrounding environment, Qs is the power absorbed by the solvent, I is the incident laser power (1.35 W/cm^2), and A_λ is the absorbance of the M-HMnO$_2$@ICG aqueous dispersion at 808 nm.

Assessment of M-HMnO$_2$@ICG's O$_2$ Generation Efficiency

To test the extracellular O$_2$ production ability of M-HMnO$_2$@ICG, the fluorescence signal of proportional [Ru (dpp)$_3$] Cl$_2$ (RDPP) bursting by O$_2$ was examined. An RDPP (10 mM, 50 μL) ethanol solution was added to PBS containing M-

$HMnO_2$@ICG (100 μg/mL). RDPP, RDPP + H_2O_2, RDPP + M-$HMnO_2$@ICG (pH 7.4), RDPP + M-$HMnO_2$@ICG + H_2O_2 (pH 7.4), RDPP + M-$HMnO_2$@ICG + H_2O_2 (pH 6.0), and H_2O_2 (100 μM) were added to the corresponding systems. At 0, 3, 6, 9, and 12 min post-reaction, each mixture was transferred to a fluorescent dish for the detection of the fluorescence intensity of RDPP (λ_{ex} = 455 nm, λ_{em} = 615 nm).

In-Vitro Photodynamic Property Assessment

To investigate the photodynamic properties of M-$HMnO_2$@ICG, the $^1O_2$ produced in each reaction system under 808 nm laser irradiation was detected using 9,10-anthracenediyl-bis(methylene)dimalonic acid (ABDA). The samples were dispersed in 1 mL PBS containing 200 μM ABDA. Under the conditions of pH 7.4, pH 7.4 + H_2O_2, and pH 6.0 + H_2O_2, 808 nm (1.35 W/cm^2) laser irradiation was applied for 2, 4, 6, 8, and 10 min. The supernatants were then collected and changes in the ABDA absorption peaks were detected using UV/Vis-NIR absorption spectroscopy.

Extracellular •OH Detection

To evaluate the responsive degradation and generation of •OH in the tumor microenvironment by the M-$HMnO_2$@ICG NPs (100 μ g/mL), GSH (0, 1, 5, and 10 mM), H_2O_2 (4 mM), $NaHCO_3$/5% CO_2 buffer solution (25 mM), and MB (10 μg/mL) were reacted under a constant temperature of 37°C for 30 min. Changes in MB absorbance at 664 nm were monitored to detect the rates of •OH generation under different conditions. Then, M-$HMnO_2$@ICG (100 μg/mL) was placed in a buffer solution (pH 6.0 or 7.4) containing $NaHCO_3$/5% CO_2 and H_2O_2 (4 mM) for 30 min, and MB degradation was assessed to determine the production of • OH through an Mn^{2+}-mediated Fenton-like reaction.

In vitro Release Experiment of ICG

Disperse M-$HMnO_2$@ICG (1 mg) in different simulated biological environments such as pH 7.4; pH 6.0; pH 6.0 + 1 mM H_2O_2; pH 6.0 + 10 mM GSH, and incubate at 37°C for various times. Then, centrifuge the solution, collect 1 mL of the supernatant for analysis by UV/Vis-NIR absorption at 800 nm, and replace with fresh buffer.

Cell Culture

HeLa cells and mouse monocyte macrophage leukemia (RAW264.7) cells were purchased from Xiangya Cell Center (Changsha, China). The cells were cultured in modified Eagle medium (MEM) and Roswell Park Memorial Institute 1640 medium, respectively, supplemented with 10% fetal bovine serum and 1% penicillin-streptomycin supplementation under 5% CO_2 at 37°C.

Assessment of in-vitro Targeting Capacity and Macrophage Phagocytic Escape

HeLa or RAW264.7 cells were inoculated in 35-mm confocal dishes (4×10^4 cells/dish) and incubated overnight, followed by the addition of 100 μg/mL $HMnO_2$@ICG or M-$HMnO_2$@ICG for 6 h. Before the experiment, the unabsorbed NPs were washed three times with PBS, 4% paraformaldehyde was added, and the mixtures were stored at 4°C for 1 h. The excess paraformaldehyde was aspirated and placed in 5 μg/mL Hoechst dye for 10 min, followed by three washes and observation under a confocal laser microscope (LSM780NLO; Zeiss, Oberkochen, Germany). Fluorescence quantification was performed using a flow cytometer (LSRFortessa; BD, USA) and the method described above.

Cytotoxicity and Inflammation Factor Detection Experiment

The cytotoxicity and therapeutic effects of the nanomaterials were tested by CCK8 assay. HeLa cells were incubated in 96-well plates at 37°C for 24 h. Then, 100 μL fresh medium containing the same concentration gradients of M-$HMnO_2$ @ICG and $HMnO_2$@ICG was added to each experimental well. After 6 h incubation, the cells were gently washed and incubation was continued for 12 h. Then, 10 μL CCK8 was introduced into each well and incubation was continued for 1 h. Cell viability was determined by measuring UV–Vis absorbance at 450 nm with a microplate reader (Unlimited M200 pro; Tecan, AT). To verify the materials' therapeutic effects, cells were cultured as described above. They were then co-incubated with M-$HMnO_2$@ICG under pretreatment conditions for 6 h, followed by laser irradiation (808 nm, 1.35 W/

cm^2, 10 min) and incubation for another 12 h. Finally, cell viability was assessed using the CCK8 method and synergistic treatment effects were evaluated. Use polymerase chain reaction to detect the effects of the photothermal effect of nanomaterials on inflammation in the microenvironment. Seed HeLa cells and RAW 264.7 macrophages separately in a 24-well plate at densities of 4×10^4 and 1×10^4 cells per well, respectively, and culture for 24 hours. After that, add different formulations to the HeLa cells and incubate for 6 hours, wash three times with PBS, and then treat the HeLa cells with an 808 nm NIR laser at an intensity of 1.35 W/cm^2 for 10 minutes. Collect the supernatant from the HeLa cells and use it to culture the RAW 264.7 macrophages for 24 hours. Then, collect the resulting RAW 264.7 cells for total RNA extraction, and further perform RT-PCR detection using a qRT-PCR kit. The primer sequences are designed according to Table S1.

Live-Dead Cell Staining and Assessment of Apoptosis

Cytotoxicity was evaluated in the control, NIR, $HMnO_2$@ICG, ICG + NIR, $HMnO_2$@ICG + NIR, and M-$HMnO_2$@ICG + NIR groups using calcein-acetoxymethyl ester (AM)/propidium iodide (PI) dye. Each well of a 24-well culture plate containing 500 μL medium was inoculated with 4×10^4 HeLa cells. When the cell confluence had reached about 70%, fresh medium containing different NPs was added and the cells were co-incubated for 6 h. Then, the cells were irradiated (808 nm, 1.35 W/cm^2, 10 min), followed by incubation for 12 h. They were then stained for 30 min using a calcein-AM /PI double staining kit and photographed under a fluorescence microscope. To quantify apoptosis, cells were cultured and treated as described above, then stained using an annexin V-Alexa Fluor 647/PI apoptosis detection kit and analyzed by flow cytometry.

Intracellular Oxygen, Glutathione, and Reactive Oxygen Species Detection

To verify intracellular O_2 production, HeLa cells were first inoculated in 24-well plates for 24 h, and then co-incubated with 10 μg/mL RDPP for 4 h. After being washed three times with PBS, they were incubated with fresh medium containing 100 μg/mL M-$HMnO_2$@ICG or $HMnO_2$@ICG for 8 h. Intracellular O_2 levels were determined by fluorescence based on RDPP signals ($\lambda_{ex}/\lambda_{em}$ = 488/600–700 nm).

To determine the effect of nanomaterial-generated O_2 on hypoxia-inducible factor-1α (HIF-1α) expression, HeLa cells were inoculated in 6-well plates at a density of 1×10^5 cells/well with 2 mL MEM for 24 h, then incubated with intact MEM containing M-$HMnO_2$@ICG or $HMnO_2$@ICG (100 μg/mL) for 8 h. After two washes with PBS, the cells were lysed and intracellular HIF-1α levels in cells treated with PBS and the two NPs were determined by Western blotting as described in our previous work.[46]

To determine the intracellular GSH content, HeLa cells were inoculated in 6-well plates at a density of 1×10^5 cells/well and incubated for 24 h. After incubation with PBS and M-$HMnO_2$@ICG (50 or 100 μg/mL) for 6 h, the medium was removed and the cells were washed three times with PBS. Then, 80 μL Triton-X-100 lysis buffer (0.4%) was added to the lysed cells. The lysate was centrifuged at 6000 rpm for 5 min, and 50 μL supernatant was mixed with 200 μL 5.5′-dithiobis-(2-nitrobenzoic acid) (0.5 mM); Absorbance at 410 nm was measured using a microplate reader.

For the ROS assay, HeLa cells were inoculated in 24-well plates at a density of 4×10^4 cells/well for 24 h. Then, samples in the control, NIR, $HMnO_2$@ICG, ICG + NIR, $HMnO_2$@ICG + NIR, and M-$HMnO_2$@ICG + NIR treatment groups were co-incubated with the respective NPs for 6 h. The cells were washed with PBS and stained with diacetyldichlorofluorescein (DCFHDA, 10 μM) at 37°C for 30 min, then laser irradiated (808 nm, 1.35 W/cm^2, 10 min), washed three times with PBS, and observed under a fluorescence microscope. In addition, HeLa cells were inoculated in 24-well plates, and ROS production in the same treatment groups was detected by flow cytometry.

Animal and Tumor Models

Nude BALB/c mice (6–8 weeks old, 18–20 g) were obtained from Hunan Silaike Experimental Animal Co. All animal experiments were approved by the Laboratory Animal Ethics Committee of Central South University (no. CSU-2023-0227) and were conducted in accordance with the Law of the People's Republic of China on the Use of Laboratory Animals. HeLa cells were collected and dispersed in PBS (3×10^7/mL), then injected subcutaneously into the right

axillae of the mice to establish a tumor-bearing model. When the tumor volume had reached 100 mm^3, the mice were used in the experiments.

Hemolysis Assay

Blood samples were obtained from normal nude BALB/c mice and centrifuged (3000 rpm, 4°C). The obtained erythrocytes were washed several times until the supernatant was clear, and a 2% (v/v) erythrocyte suspension was prepared with PBS. This suspension (200 μL) was added to a series of equal volumes of M-$HMnO_2$@ICG at concentrations of 12.5, 25, 50, 100, and 200 μg/mL and co-incubated at 37°C for 2 h. It was then centrifuged at 10,000 rpm, and 100 μL supernatant was transferred to each well of a 96-well plate. Absorbance at 540 nm was measured and the hemolysis rate was calculated using the optical density (OD) and the following formula: hemolysis rate (%) = $OD_{sample} - OD_{negative\ control}$ / $OD_{positive\ control} - OD_{negative\ control} \times 100$.

In-Vivo and Ex-Vivo Fluorescence Imaging

Tumor-bearing mice were injected in the tail vein with 100 μL $HMnO_2$@ICG and M-$HMnO_2$@ICG at the same concentration (400 μg/mL). At 0, 12, 24, 48, and 72 h post-injection, the mice were anesthetized with gas and in-vivo fluorescence imaging was performed using a small-animal imaging system (Ani View 600; $\lambda_{ex}/\lambda_{em}$ = 745/840 nm). For ex-vivo fluorescence imaging, all mice were executed 72 h after injection, and the tumors and major organs (heart, liver, spleen, lungs, and kidneys) were dissected, washed with PBS, and examined using the in-vivo imaging system.

In-Vivo and in-vitro Magnetic Resonance Imaging

The in-vitro T1-weighted imaging properties of M-$HMnO_2$@ICG were examined using a 7.0-T MRI scanner. Samples containing different concentrations (0.1725, 0.345, 0.69, and 1.38 mM) of Mn^{2+} were dispersed in PBS (pH 6.0 or 7.4), and GSH (10 mM) or H_2O_2 (1 mM) was added. T1 relaxation rates were obtained by detecting the T1 signal intensity in each group. For in-vivo MRI examination, M-$HMnO_2$@ICG (20 mg/kg) was injected (intravenous or intratumor) into HeLa tumor (~100 mm^3)–bearing mice. For the intratumor injection model, MRI was performed on mice that had not been injected and on treated mice at 30 min and 1 h after injection. For the intravenous injection model, MRI was performed in the tumor region on mice that had not been injected and on treated mice 24 h after injection.

Biodistribution Measurements

Hela tumor-bearing mice were divided into three groups (n=3), and dissected at 12, 24, and 48 hours post-injection to collect tumor tissues. Subsequently, all tumor tissues were treated with concentrated nitric acid and heated until the solution became clear. The manganese content in the solution was determined using an Inductively Coupled Plasma Optical Emission Spectrometer (ICP-OES), and the manganese content in the collected mouse tumor tissues was calculated.

In-Vivo Photothermal Imaging

$HMnO_2$@ICG or M-$HMnO_2$@ICG (Mn^{2+} concentration, 20 mg/kg) was injected into tumor-bearing mice. Twenty-four hours after injection, the mice were anesthetized for tumor site irradiation (808 nm, 1.35 W/cm^2, 3min) and infrared thermal imaging (ONE PRO; FLIR). Tumor site warming was monitored.

In-Vivo Examination of Antitumor Treatment Effects

HeLa tumor (~100 mm^3)–bearing nude BALB-c mice were divided randomly into six treatment groups (n = 3 each): PBS, NIR, ICG + NIR, $HMnO_2$@ICG, $HMnO_2$@ICG + NIR, and M-$HMnO_2$@ICG + NIR. The nanomedicines were injected through the tail vein on days 0 and 5 of the treatment cycle, according to the previously determined time window of maximum drug accumulation. Twenty-four hours after injection, all animals were anesthetized and irradiated (1.35 W/cm^2, 3 min). The animals' weight and tumor volume were monitored and recorded every other day during the treatment

period. After 14 days, the mice were euthanized and representative tumor tissue samples were collected, photographed, and weighed. The tumor tissues and major organs of mice from the different treatment groups were stained with hematoxylin and eosin (H&E), and mouse tumor tissues were stained by terminal deoxynucleotidyl transferase dUTP nick end labeling (TUNEL) to detect apoptosis. To detect HeLa cell hypoxia, tumor tissues from each treatment group were stained with anti–HIF-1α antibody, washed with PBS to remove the primary antibody residue, and then incubated with goat anti-rabbit immunoglobulin G at 37°C for 1 h. Fluorescence was then observed, with green fluorescence representing hypoxic areas.

Biosafety Analysis

To examine the biosafety of M-HMnO_2@ICG, mice that had undergone 14 days of the different treatments were euthanized, blood samples were collected, and serum specimens were obtained by centrifugation. Biochemical assays were performed to determine the aspartate aminotransferase, alanine aminotransferase, total protein, albumin, blood urea nitrogen, creatinine, total cholesterol, and triglyceride levels.

Statistical Analysis

The data are expressed as means ± standard deviations. GraphPad Prism 8 was used for the statistical calculations and plotting. One-way and two-way analyses of variance were used to compare data from the various treatment groups. $P < 0.05$ was considered to indicate significance.

Results and Discussion

M-HMnO_2@ICG NP Preparation and Characterization

Firstly, an oxidation-reduction reaction occurs between $KMnO_4$ and SiO_2, resulting in the formation of a MnO_2 layer on the surface of well-dispersed SiO_2NPs (Figure 1A), thus creating SiO_2-MnO_2 NPs (Figure 1B). Then, utilizing the strong alkaline properties of Na_2CO_3 as an etching agent, the internal silicon shell is dissolved to prepare $HMnO_2$ NPs. TEM observation confirmed that all prepared NPs had regular spherical structures and sizes of about 110 nm. The $HMnO_2$ NPs had typical hollow structures (Figure 1C). Elemental scanning analysis revealed significantly reduced silicon elemental signals in the $HMnO_2$ structure relative to SiO_2-MnO_2 (Figure S1), confirming the successful etching of the silicon shells. Significant Mn elemental signals were observed in the $HMnO_2$ structure (Figure S2), confirming the synthesis of the MnO_2 shells. BET calculations yielded a specific surface area of 178 m^2/g and average pore size of 4 nm for $HMnO_2$ (Figure 1D), conforming to a typical type-IV Langmuir isotherm and indicating the presence of a large hollow structure and abundant mesopores to facilitate drug adsorption and loading.

After HMnO_2@ICG synthesis, TEM observation revealed blurring of the hollow NP structure and cluster-like aggregation around the core-shell structure (Figure 1E). Elemental mapping images and corresponding X-ray energy-dispersive spectra confirmed the existence and spatial distribution of Mn, O, N, P, and S in HMnO_2@ICG (Figure 1F), thereby confirming phosphate-mediated ICG encapsulation.

Under consistent reaction conditions, we investigated the effect of different carrier modifications on the drug loading capacity and encapsulation efficiency of ICG. We observed that, compared to the samples with $HMnO_2$ and $HMnO_2$/PAH as carriers, the group treated with $HMnO_2$/PAH/HPO_4^{2-} as the carrier exhibited the lowest ultraviolet/visible-near infrared in the supernatant (Figure 1G). The UV/Vis-NIR absorption of the supernatant indicated the presence of unencapsulated (free) ICG. Quantitative analysis was conducted by examining the linear relationship between the characteristic peak and concentration of ICG dissolved in PB (Figure S3). We found that these rates were significantly higher for $HMnO_2$/PAH/HPO_4^{2-} (31.72% and 95.14%, respectively) than for $HMnO_2$ (5.43% and 24.16%, respectively) and $HMnO_2$/PAH (17.21% and 68.58%, respectively; Figure 1H), attributable mainly to the high ICG affinity of the counterion aggregation effect formed by phosphate/PAH.

TEM observation showed that the encapsulated HMnO_2@ICG NP surfaces had a clear lipid layer with a thickness of about 8.6 nm (Figure 1I). DLS measurement showed that the NP size had increased from 240 to 258 nm after cell membrane encapsulation (Figure 1J). The synthesis of M-HMnO_2@ICG was verified by zeta potential monitoring. The

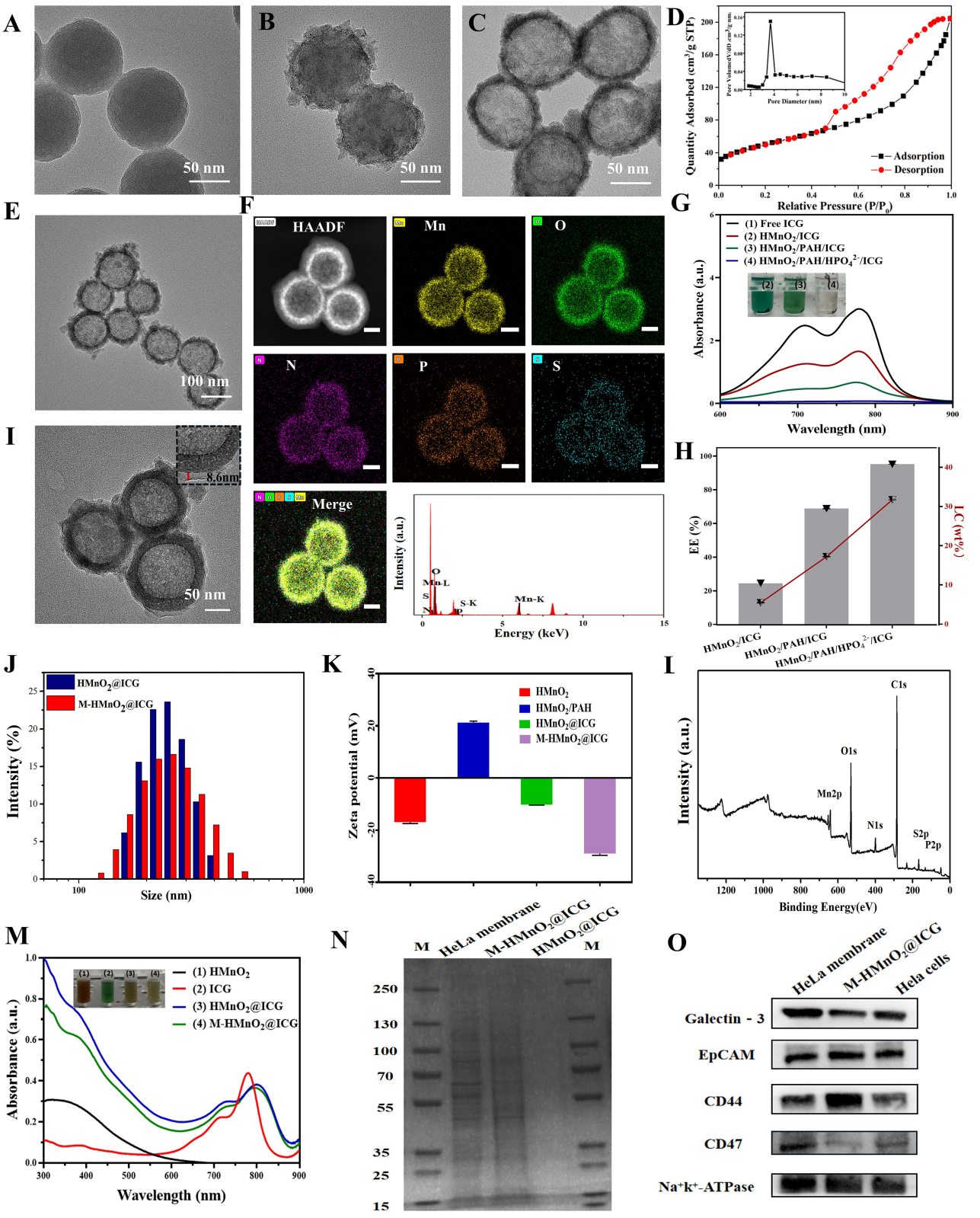

Figure 1 (**A**–**C**) Transmission electron microscopic images of SiO_2, SiO_2@MnO_2, and $HMnO_2$ nanoparticles. (**D**) N_2 adsorption/desorption isotherms and pore size distribution curve (inset) for synthesized $HMnO_2$. (**E**) Transmission electron microscopic image of $HMnO_2$@ICG. (**F**) Elemental mapping images and energy-dispersive spectra of Mn, O, N, P, and S in $HMnO_2$@ICG. Scale bar: 50 nm. (**G**) Supernatant UV/Vis-NIR absorption after ICG loading of $HMnO_2$@ICG under different addition conditions. (**H**) Drug loading and encapsulation rates of ICG-loaded NPs under different conditions. (**I**) Transmission electron microscopic image of M-$HMnO_2$@ICG. (**J**) Hydrodynamic dimensions of $HMnO_2$@ICG and M-$HMnO_2$ @ICG, determined by DLS measurement. (**K**) Surface charges of $HMnO_2$, $HMnO_2$/PAH, $HMnO_2$@ICG, and M-$HMnO_2$@ICG. Data are expressed as means ± standard deviations (n = 3). (**L**) Full XPS characteristics of M-$HMnO_2$@ICG. (**M**) UV/Vis-NIR absorption spectra of $HMnO_2$, ICG, $HMnO_2$@ICG, and M-$HMnO_2$@ICG. (**N**) SDS-PAGE results for HeLa cell membranes, M-$HMnO_2$@ICG, and $HMnO_2$@ICG. (**O**) Western blots of HeLa cells, their membranes, and M-$HMnO_2$@ICG.

potential of $HMnO_2$@ICG changed from +21 to –10 mV, suggesting the occurrence of a flip relative to the $HMnO_2$/PAH potential that was attributed to successful ICG loading. The M-$HMnO_2$@ICG NP charge was further reduced to –29 mV relative to that of $HMnO_2$@ICG after cell membrane encapsulation, which may be attributed to the cell membrane surface charge (Figure 1K).

X-ray photoelectron spectroscopy (XPS) detected absorption peaks for Mn, O, N, P, and S in M-$HMnO_2$@ICG (Figure 1L). The high-resolution XPS spectrum of Mn2p showed peaks at 642.3 and 653.3 eV (Figure S4) corresponding to the bonding energies of $Mn2p_{3/2}$ and $Mn2p_{1/2}$ of MnO_2, respectively, the satellite peak of manganese (Mnsat)is located approximately 3 eV higher in energy than the main peak, indicating the presence of manganese in a higher oxidation state.[47]

The high-resolution XPS spectrum of S2p showed $2p_{1/2}$ and $2p_{3/2}$ peaks corresponding to the bonding energy of the sulfonic acid moiety[48] (-SO_3H, ~169 eV; Figure S5), with the N and P peaks attributed to the PAH/phospholipid bilayer-coated cell membranes and the presence of HPO_4^{2-}, respectively (Figure S6 and S7). UV/Vis-NIR absorption spectral peaks for the M-$HMnO_2$@ICG and $HMnO_2$@ICG NPs were consistent with those for the $HMnO_2$ NPs at 300–500 nm and ICG at 700–850 nm (Figure 1M). In particular, the red-shifted ICG peaks of $HMnO_2$@ICG were ascribed to the conversion of ICG monomers to J aggregates via non-covalent chemistry.[49] The characteristic ICG absorption peaks of M-$HMnO_2$@ICG were consistent with those of $HMnO_2$@ICG, indicating that the ICG-loaded NPs maintain functional integrity after physical coextrusion and cell membrane encapsulation.

The integrity of surface proteins after $HMnO_2$@ICG NP encapsulation was examined further. The protein bands of the M-$HMnO_2$@ICG NPs were almost the same as those of the HeLa cell membranes; no protein band was detected for $HMnO_2$@ICG (Figure 1N). Several marker proteins were detected on the HeLa cell surfaces, including isotype-targeting highly dependent cell adhesion molecules (eg, epithelial cell adhesion molecule, galectin-3, CD44, and CD47). CD44, a signature tumor-cell transmembrane glycoprotein, is involved in heterogeneous tumor cell adhesion.[50] CD47, a transmembrane glycoprotein that is expressed and up-regulated widely in tumor cells, binds to signal-regulatory protein-α on the surfaces of macrophages and signals to inhibit macrophage phagocytosis, thereby playing an important role in immune escape.[51,52] These proteins were preserved on the surfaces of the HeLa cells, their membranes, and the M-$HMnO_2$@ICG NPs, indicating that NP preparation by co-extrusion did not disrupt their presence (Figure 1O). Western blotting confirmed that these homologous targeting- and immune tolerance–associated proteins had been transferred from the cell membranes to the NP surfaces, providing the basis for the NPs' action.

M-$HMnO_2$@ICG Photothermal, Photodynamic, and Chemical Kinetic Properties, and Degradation Properties Reflecting Tumor Microenvironment Responsiveness

As the ICG loaded on M-$HMnO_2$@ICG showed significant absorption in the 700–900-nm NIR spectral region, indicating that this NP had the property of a photothermal reagent, we systematically investigated its in-vitro photothermal properties. The photothermal conversion temperatures of M-$HMnO_2$@ICG solutions with different concentrations under 6 min NIR irradiation showed obvious concentration dependence; a temperature of 25°C was achieved with a concentration of 200 μg/mL, relative to 3°C for water (control; Figure 2A). The relationship between warming and laser power was also investigated. The temperature of M-$HMnO_2$@ICG (150 μg/mL) under 6 min irradiation increased with the laser power density (Figure 2B), indicating that this NP effectively converted 808 nm laser energy into thermal energy. We further investigated the photothermal stability and conversion efficiency of M-$HMnO_2$@ICG. In the on/off cycle irradiation (808 nm) experiment, M-$HMnO_2$@ICG showed no obvious temperature attenuation after four cycles, indicating good photothermal stability (Figure 2C). Photothermal conversion efficiency is the efficiency with which a photothermal agent converts absorbed energy from near-infrared light into thermal energy, and is a key parameter for evaluating the performance of photothermal agents. The photothermal conversion efficiency of the M-$HMnO_2$@ICG solution, calculated by fitting the curve of temperature change over time during cooling, was 34.62% (Figure 2D). An infrared thermal imager was also used to obtain photothermal images of M-$HMnO_2$@ICG solutions with different concentrations. The solution color changed from light-yellow to light-red with increasing concentration and irradiation time (Figure 2E), confirming the preparation's photothermal conversion efficiency.

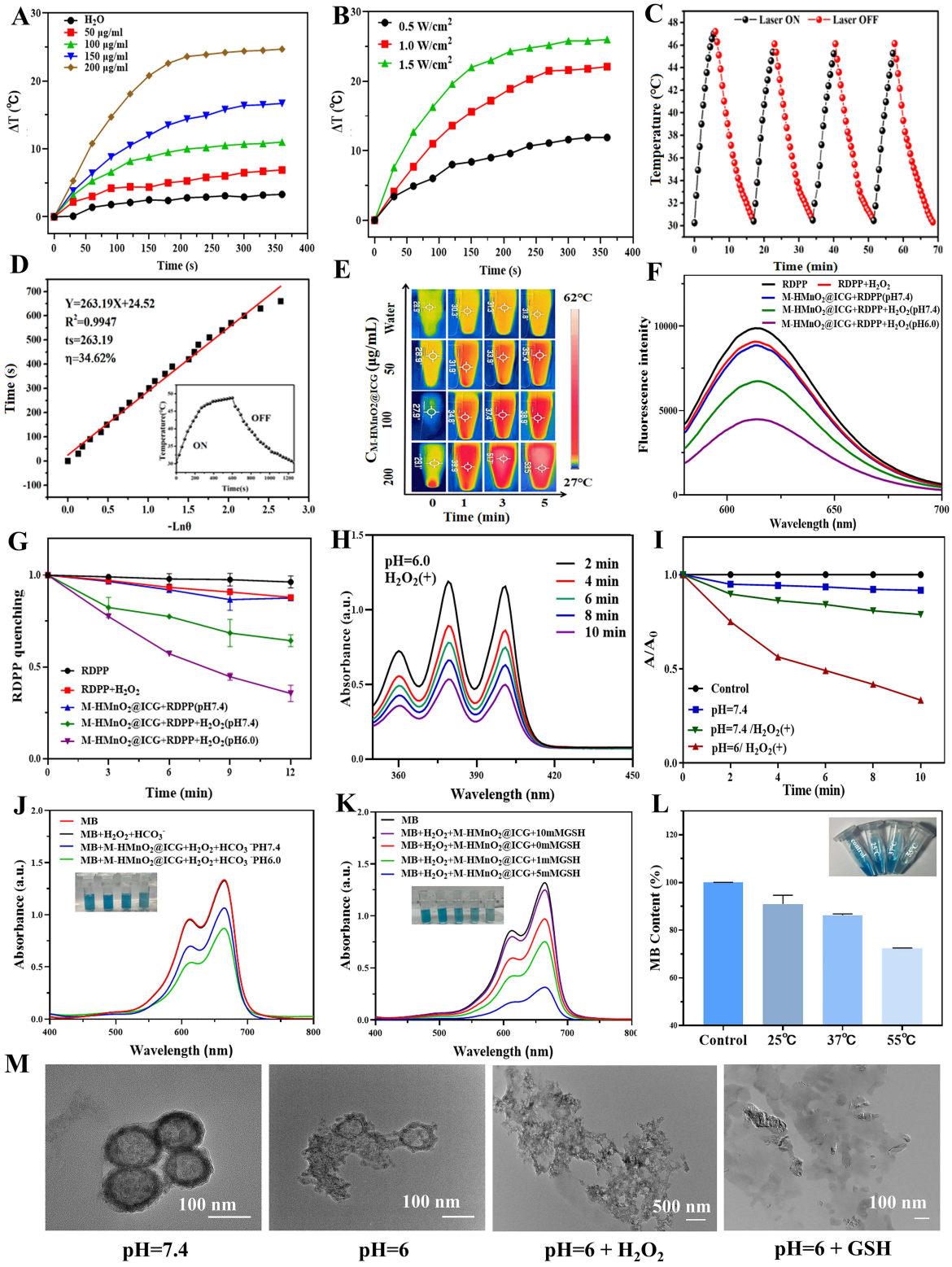

Figure 2 (**A**) In-vitro photothermal properties of M-HMnO$_2$@ICG nanoparticles; temperature curves for different concentrations of M-HMnO$_2$@ICG under 808-nm laser irradiation for 6 min. (**B**) Temperature curves for M-HMnO$_2$@ICG solution (150 μg/mL) under 808-nm laser irradiation at different power densities. (**C**) Photothermal conversion of M-HMnO$_2$@ICG solution (150 μg /mL) over four on/off irradiation (808 nm) cycles. (**D**) Photothermal properties of aqueous M-HMnO$_2$@ICG solution and their linear relationship with time; temperature curve for M-HMnO$_2$@ICG (150 μg/mL) under laser irradiation (808 nm, 1.35 W/cm^2, 600 s; inset). (**E**) Infrared thermography of aqueous M-HMnO$_2$@ICG solutions under 808-nm (1.35 W/cm^2) laser irradiation for 0–5 min. (**F**) Fluorescence (RDPP probe) under different conditions reflecting M-HMnO$_2$@ICG O_2 generation and (**G**) O_2 production over time. (**H**) Variation in ABDA absorbance of M-HMnO$_2$@ICG nanoparticles in pH 6.0 + H_2O_2 solution with different laser irradiation intervals. (**I**) Normalized ABDA absorbance under different conditions. UV–Vis absorption spectra of supernatants after (**J**) warming in different pH buffer solutions and (**K**) incubation with different GSH concentrations. (**L**) MB degradation and photograph of the same samples after different temperature treatments (inset). (**M**) Nanoparticle degradation under different conditions, observed by transmission electron microscopy.

Next, We used RDPP as a probe to investigate the O_2 production capacity of M-HMnO_2@ICG NPs. As the fluorescence of RDPP is quenched upon reaction with O_2, decreases in its fluorescence signal can be used as O_2 level markers. Among treatment groups, RDPP + M-HMnO_2@ICG + H_2O_2 (100 μM) showed the most pronounced decrease in fluorescence in the reaction system with buffer solution of pH 6.0, demonstrating the NP's ability to produce O_2 (Figure 2F). We further investigated reaction kinetics and observed no significant fluorescence quenching within 12 min for RDPP, RDPP + H_2O_2, or RDPP + M-HMnO_2@ICG (pH 7.4; Figure 2G). At pH 7.4, the fluorescence quenching of RDPP + M-HMnO_2@ICG + H_2O_2 was slow relative to that at pH 6.0, consistent with the postulated reaction of MnO_2 with H_2O_2 to generate more O_2 in an acidic environment. These findings indicate that the NPs self-produced O_2 in the in vitro-simulated tumor microenvironment, providing for ICG-mediated PDT. ICG produces ROS ($^1O_2$) under photodynamic action. We used ABDA as a probe to examine the photodynamic performance of ICG. $^1O_2$ can oxidize ABDA to peroxides, reducing its UV absorption at 380 nm. At pH 7.4, the typical ABDA absorption peak in the M-HMnO_2@ICG solution remained almost unchanged with 10 min laser irradiation (Figure S8), indicating that the NP had weak photodynamic properties. With the addition of H_2O_2 to the solution, the ABDA absorption peak decreased more (Figure S9) because the small amount of O_2 generated by catalysis under this condition enhanced the photodynamic efficiency of ICG. At pH 6.0, the ABDA absorption peak of M-HMnO_2 @ICG decreased significantly with increasing irradiation time (Figure 2H). UV absorption was measured at 380 nm for relative quantification and the more intuitive characterization of the photodynamic properties of ICG under different conditions (Figure 2I). These results indicate that M-HMnO_2@ICG produced O_2 through CAT-like activity in the acidic, H_2O_2-rich tumor microenvironment, providing substrates for ICG and enhancing its photodynamic effects.

In addition to increasing the photodynamic effect through catalytic O_2 production, MnO_2 can be degraded to generate Mn^{2+}. MB was used as an indicator for ·OH detection to study the chemical kinetic properties of M-HMnO_2@ICG. H_2O_2 and M-HMnO_2@ICG were added to $NaHCO_3$ buffer containing MB and incubated for 30 min, and the MB absorbance in the supernatant was then detected. The fluorescence signal was significantly weaker with pH 6.0 buffer solution than with pH 7.4 buffer solution (Figure 2J), indicating that the chemical kinetic effect was stronger in an acidic simulated tumor microenvironment. Absorbance did not differ significantly between the MB alone (control) and MB + H_2O_2 + HCO_3^- groups, indicating that no ·OH was generated without the addition of nanomaterials. As MnO_2 can degrade rapidly, producing Mn^{2+}, under GSH-rich conditions in cells, we investigated the effect of nanomaterials and GSH reactions on MB degradation. The UV-Vis absorption of MB decreased gradually, reflecting more Mn^{2+} production and thus a stronger chemical kinetic effect, with increasing GSH concentration (Figure 2K). The rates of Fenton-like reactions and ·OH generation increased with the temperature (Figure 2L), indicating that the photothermal effect of ICG has a synergistic effect on chemical kinetics.

To visually assess M-HMnO_2@ICG degradation in the simulated tumor microenvironment, we incubated the NP in buffer solutions of pH 7.4, pH 6.0, pH 6.0 + H_2O_2, and pH 6.0 + GSH for 2 h and then observed them under a TEM. The structure of M-HMnO_2@ICG remained relatively intact in the pH 7.4 buffer solution (Figure 2M), demonstrating stability during in-vivo cycling. In the slightly acidic (pH 6.0) environment, the NPs tended to collapse, losing their original morphology. After the addition of H_2O_2 or GSH, the NP morphology changed significantly, with degradation into smaller nanoclusters. Additionally, under conditions of pH 6, pH 6.0 + H_2O_2, and pH 6.0 + GSH, the cumulative release of ICG is significantly greater than under conditions of pH 7.4 (Figure S10). These results indicate that the designed nanomaterials have the property of tumor microenvironment–responsive release, enabling effective synergistic PTT/PDT/CDT.

In-Vitro Tumor Targeting and Immune Escape Properties of M-HMnO_2@ICG

In this study, NPs were coated with tumor cell membranes with the aim of enabling them to evade macrophage-mediated nonspecific clearance, prolong the circulation time in the bloodstream, enhance interaction with tumor cells, and achieve homologous targeted delivery to tumor cells. To verify the effectiveness of this approach, we used RAW cells as phagocytes and HeLa cells as targets to study phagocytic escape and homologous uptake of M-HMnO_2@ICG NPs by confocal laser scanning microscopy. In examining the efficacy of cell membrane encapsulation, we used HMnO_2@ICG without encapsulation as a control.

We used the spontaneous fluorescence of ICG to trace the NPs and 4',6-diamidino-2-phenylindole staining of nuclei to localize cells. HeLa cells treated with M-HMnO$_2$@ICG showed significantly more red fluorescence than did those incubated with HMnO$_2$@ICG (Figure 3A), confirming the good targeting of M-HMnO$_2$@ICG to homologous tumor cells. Mouse macrophages (RAW264.7 cells) co-incubated with HMnO$_2$@ICG showed weak red fluorescence and those co-incubated with M-HMnO$_2$@ICG showed almost none, indicating that the designed NPs have a certain immune escape effect (Figure 3B). HeLa and RAW cells were co-incubated with HMnO$_2$@ICG and M-HMnO$_2$@ICG, respectively, and nanomaterial uptake was examined using flow cytometry. The fluorescence intensity of HeLa cells co-cultured with M-HMnO$_2$@ICG was 26.9% greater than that of those co-cultured with HMnO$_2$@ICG (Figure 3C). The fluorescence intensity of RAW264.7 cells co-cultured with M-HMnO$_2$@ICG was only 52.6% of that of cells co-cultured with HMnO$_2$@ICG (Figure 3D). The fluorescence imaging and flow cytometry results (Figure 3E)were consistent and indicate that the proteins on the tumor cell membrane surfaces prevented rapid in-vivo NP clearance through immune escape, enhancing uptake in tumor cells through homologous targeting and thereby achieving enhanced antitumor efficacy.

In-Vitro Antitumor Properties

The test tube–level experiments showed that the NPs prepared in this study had synergistic PTT/PDT/CDT properties. The effect of M-HMnO$_2$@ICG NPs on HeLa cell viability was detected by CCK8 assay to evaluate the in-vitro antitumor activity of the NPs. In the absence of light, M-HMnO$_2$@ICG and HMnO$_2$@ICG showed no significant cytotoxicity at a concentration of 100 μg/mL, confirming their biosafety. At a concentration of 200 μg/mL, a significant cell-killing effect was observed, attributable mainly to the NPs' chemical kinetic effects. The cell-killing effect of M-HMnO$_2$@ICG was significantly stronger than that of HMnO$_2$@ICG, reflecting the former's stronger tumor cell targeting (Figure 4A). Under laser irradiation (808 nm, 1.35 W/cm^2,

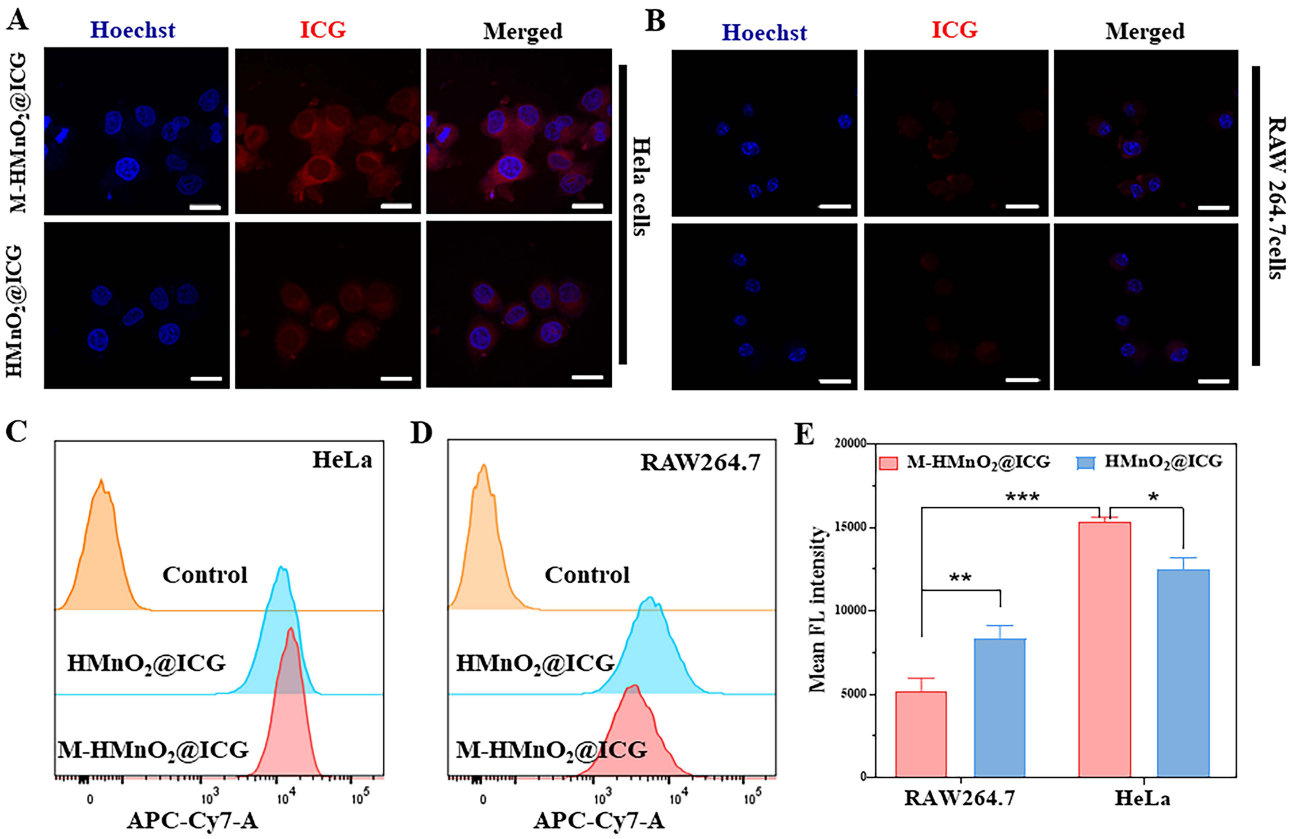

Figure 3 (**A** and **B**) Confocal laser scanning microscopic images of HeLa and RAW264.7 cells treated with HMnO2@ICG and M-HMnO2@ICG nanoparticles for 6 h (scale bar = 20 μm). (**C** and **D**) Flow cytometry images of the relative fluorescence of the same treated cells. Relative fluorescence intensity and (**E**) fluorescence quantification for the same treated cells. Data are expressed as mean ± SD (n = 3). Statistical significances were calculated via one-way analysis of variance (ANOVA).*P < 0.05,**P < 0.01, ***P < 0.001.

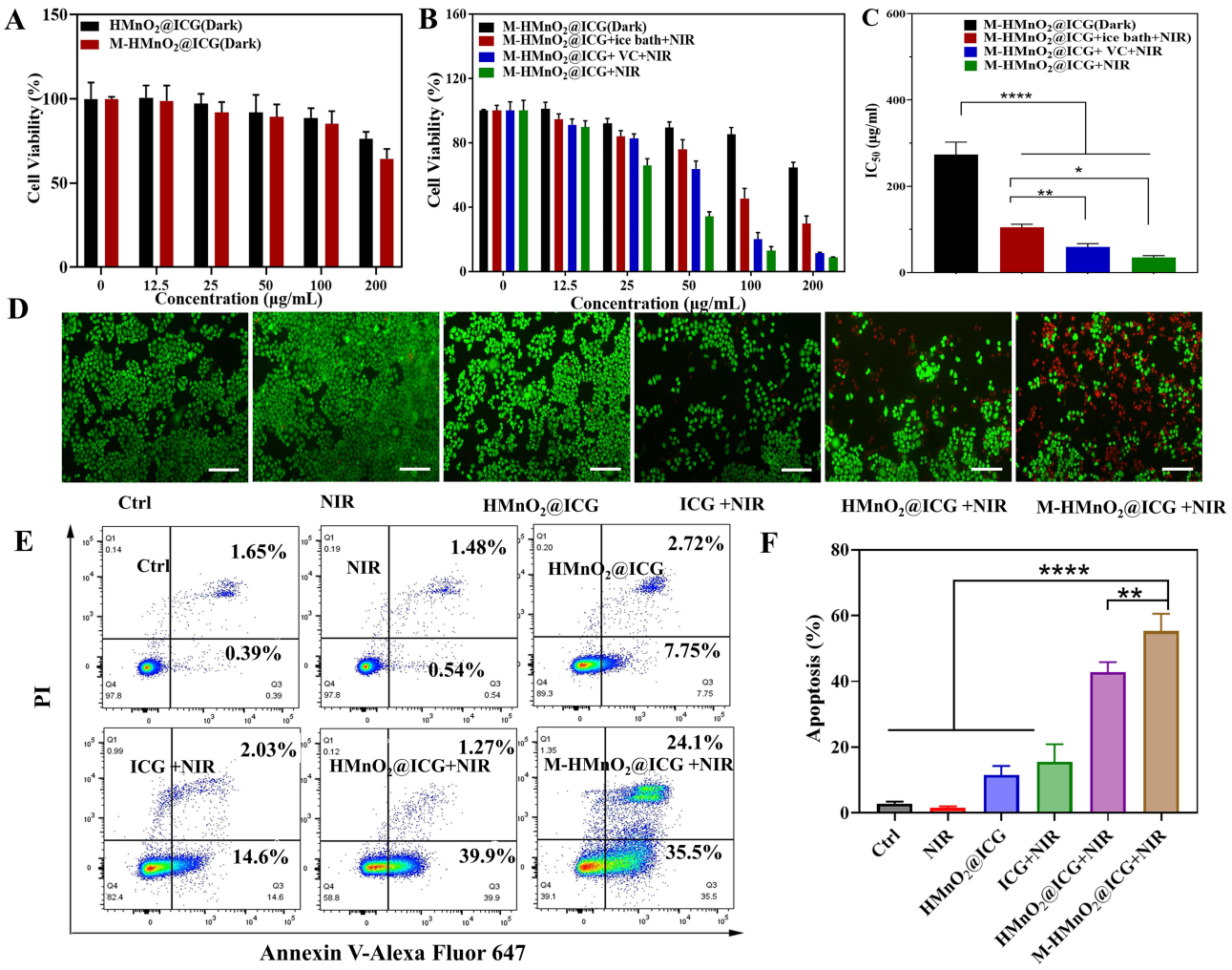

Figure 4 (**A**) Effects of different concentrations of M-HMnO$_2$@ICG and HMnO$_2$@ICG on HeLa cell viability. (**B**) HeLa cell viability after treatment with M- HMnO$_2$@ICG at different concentrations and under different conditions. (**C**) IC$_{50}$s, calculated using the data illustrated in panel B. (**D**) Live/dead HeLa cell staining after different treatments (scale bar: 50 μm). Apoptosis as determined by (**E**) flow cytometry and (**F**) quantitative analysis after different treatments. Data are expressed as mean ± SD (n = 3). Statistical significances were calculated via one-way analysis of variance (ANOVA). *P < 0.05, **P < 0.01, ****P < 0.0001.

10 min), M-HMnO$_2$@ICG had a concentration-dependent antitumor effect, suggesting a combined therapeutic effect. To further distinguish PTT, PDT, and CDT contributions, we pretreated the cells with an ice bath or vitamin C. The untreated group without laser irradiation represented the CDT effect, and the difference in cell survival between the ice bath–treated and non–laser-irradiated groups was considered to reflect the PDT contribution. The vitamin C treatment was considered to contribute to the PTT effect due to the elimination of photodynamic and chemodynamic effects. The ice bath and vitamin C pretreatments increased cell survival, confirming the synergistic contributions of photothermal, photodynamic, and chemokinetic effects to the antitumor activity of the NPs (Figure 4B). The half-maximal inhibitory concentrations (IC$_{50}$s) of M-HMnO$_2$@ICG (chemodynamic contribution), M-HMnO$_2$@ICG + ice bath (photodynamic and chemodynamic contributions), and M-HMnO$_2$@ICG + vitamin C (photothermal contribution) were 273.4, 104.9, and 59.0 μg/mL, respectively (Figure 4C). The IC$_{50}$ of M-HMnO$_2$ @ICG + NIR was the lowest (34.7 μg/mL), reflecting the combined therapeutic effect of M-HMnO$_2$@ICG with homologous targeting to promote PTT/PDT/CDT under light conditions. Considering that photothermal therapy raises the temperature of local tumor tissues and potentially triggers inflammatory responses, to assess the impact of photothermal therapy on inflammation within the tumor microenvironment, we examined the effects of treated HeLa cells on inflammatory responses in RAW 264.7 macrophages. Using real-time polymerase chain reaction, we measured the levels of inflammatory factors released by treated cells. As depicted in Figure S11, under near-infrared light conditions, both HMnO$_2$@ICG and M-HMnO$_2$@ICG did not significantly upregulate the mRNA expression of pro-inflammatory factors (TNF-α, IL-1β, and IL-6), in contrast to the ICG+NIR

group, which exhibited increased expression of IL-1β and IL-6. This finding underscores the advantage of using the nanomaterial M-HMnO$_2$@ICG over solely using ICG in the tumor microenvironment under near-infrared light exposure.

The NPs' antitumor activity was visualized by live/dead cell staining. After NIR irradiation, M-HMnO$_2$@ICG caused a large number of cell deaths (red fluorescent labeling), further confirming its combined therapeutic and targeting effects (Figure 4D). To further explore the tumor cell death pathway, we used flow cytometry and an annexin V-APC/PI apoptosis detection kit. As expected, M-HMnO$_2$@ICG + NIR triggered the strongest cell-autonomous programmed death, with an apoptosis rate of 59.6%, exceeding that observed for HMnO$_2$@ICG + NIR without tumor cell membrane encapsulation (Figure 4E and F).

Cellular-Level Validation of the Antitumor Potentiation Mechanism of M-HMnO$_2$@ICG

At the test tube level, we demonstrated that MnO$_2$ enhanced the effect of ICG via self-oxygenation and chemical kinetics. We further validated this effect at the cellular level, using RDPP to examine O$_2$ production was significantly reduced in HMnO$_2$@ICG- and M-HMnO$_2$@ICG–treated cells incubated for the same period of time compared with the control group (Figure 5A), suggesting that MnO$_2$ NPs efficiently produce O$_2$ in tumor cells by catalyzing endogenous H$_2$O$_2$. The O$_2$ production effect was more pronounced in the M-HMnO$_2$@ICG group than in the HMnO2@ICG group, which may be attributed to the former's superior cellular uptake effect. HIF-1α is a marker of the intracellular O$_2$ level; its level correlates negatively with the intracellular O$_2$ concentration. The alteration of the intracellular O$_2$ level was further clarified by measuring HIF-1α expression. The

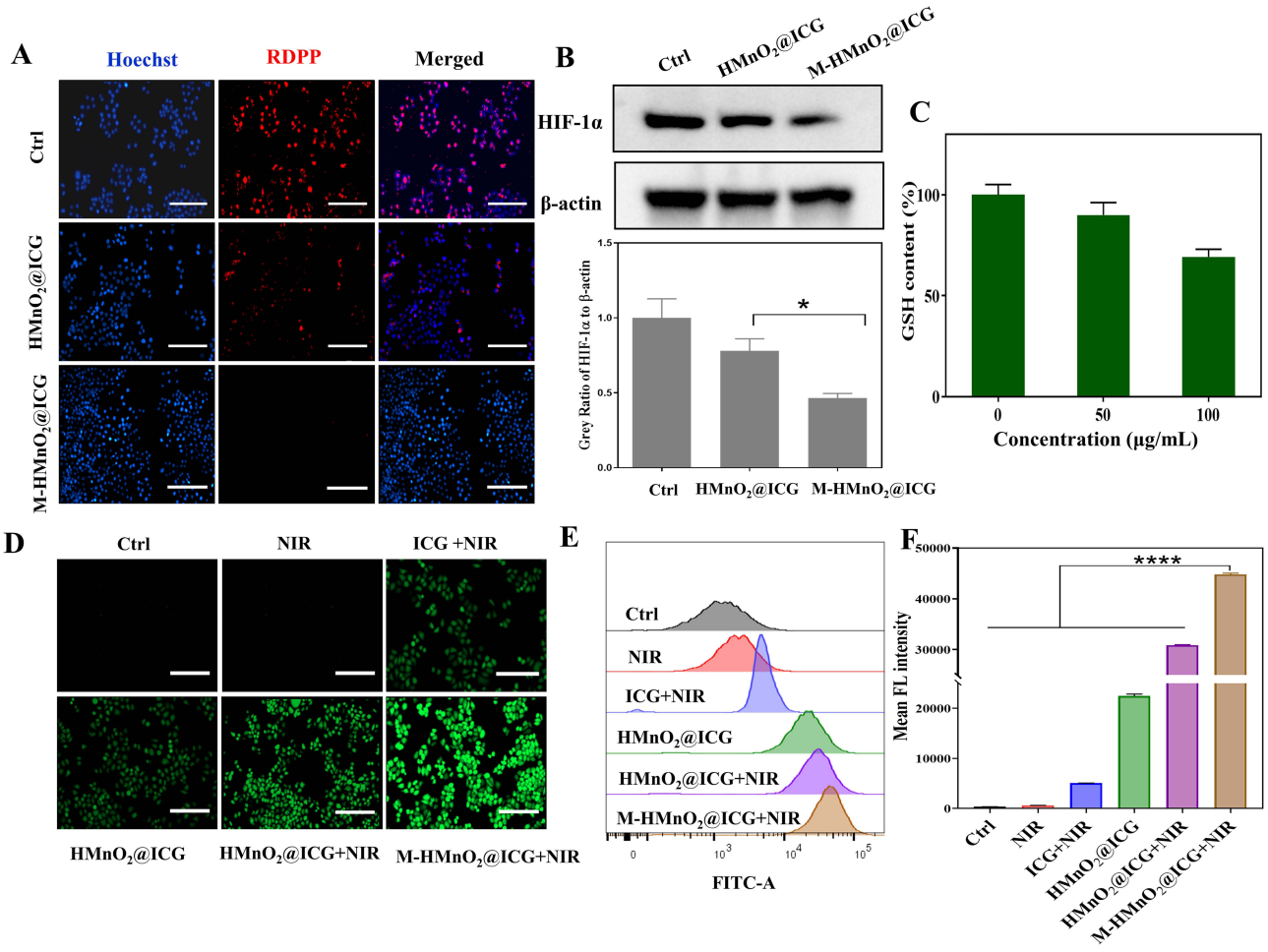

Figure 5 (**A**) Fluorescence images of RDPP staining of HeLa cells under different treatments (scale bar: 200 μm). (**B**) HIF-1α expression in Hela cells under different treatments and quantitative analysis. (**C**) Relative GSH levels in HeLa cells after treatment with different concentrations of M-HMnO$_2$@ICG. Fluorescence images of DCFHDA staining of HeLa cells after different treatments (**D**) and corresponding flow cytometry assays (**E**) and relative fluorescence intensity (**F**). The data represent mean ± SD, one-way ANOVA, *P < 0.05, ****P < 0.0001.

intracellular HIF-1α level was significantly decreased after treatment with M-HMnO$_2$@ICG and HMnO$_2$@ICG (Figure 5B), further confirming the NPs' ability to alleviate tumor hypoxia via self-oxygenation.

High GSH concentrations in tumor cells protect against oxidative stress damage, thereby reducing the tumor cell–killing effect of ROS. MnO$_2$ has been shown to react with GSH, reducing its intracellular level and enhancing the therapeutic effect of oxidative stress.[53] To demonstrate this effect, we incubated HeLa cells with different concentrations of M-HMnO$_2$@ICG and measured the intracellular GSH level by sulfhydryl tracking assay. M-HMnO$_2$@ICG reduced the intracellular GSH concentration in a concentration-dependent manner (Figure 5C). Thus, it weakens tumor cells' antioxidant defense systems, facilitating their killing through ROS generation.

We used a DCFHDA probe to detect the ROS production in HeLa cells by different NPs. The green DCFHDA fluorescence in the cells was very weak under the control and irradiation-only conditions (Figure 5D). Under laser irradiation, free ICG induced a weak fluorescent signal in HeLa cells. For HMnO$_2$@ICG in the absence of light, some fluorescent signal was generated due to the occurrence of Mn^{2+}-mediated Fenton-like reactions. Green fluorescence was strongest in the irradiated M-HMnO$_2$@ICG group, reflecting effective cellular internalization and intracellular self-oxygenation for sensitized PDT. The analysis of green fluorescence by flow cytometry (Figure 5E) and quantification (Figure 5F) produced similar results. Together, these results indicate that M-HMnO$_2$@ICG effectively targeted tumor cells and produced O$_2$ intracellularly for PDT sensitization, achieving PTT and Mn^{2+}-mediated Fenton-like effects.

In-Vivo Tumor Targeting Properties of M-HMnO$_2$@ICG

After clarifying the antitumor activity of M-HMnO$_2$@ICG at the cellular level, the performance of M-HMnO$_2$@ICG was further investigated at the animal level. M-HMnO$_2$@ICG showed <5% hemolysis, even at a concentration of 200 μg/mL (Figure S12), indicating its good biocompatibility with tail vein injection. A female nude BALB/c mouse tumor model was constructed, and the tumor-targeting properties of the nanopreparations were first evaluated using ICG fluorescence. Using an in-vivo small-animal imager, dynamic fluorescence changes in the mice after tail vein injection were observed (Figure 6A). Twelve hours after injection, fluorescence at tumor sites was detected in the M-HMnO$_2$@ICG and HMnO$_2$@ICG groups. The tumor-site fluorescence intensity peaked at 24 h and then decreased gradually, indicating that the optimal time for laser irradiation is 24 h after injection. The tumor-tissue fluorescence intensity was greater in the M-HMnO$_2$@ICG group than in the HMnO$_2$@ICG group at all timepoints, and some fluorescence was detected at 72 h in the former group, suggesting stronger tumor targeting and retention of M-HMnO$_2$@ICG. The mice were executed and their major organs and tumor tissues were collected for ex-vivo imaging, which confirmed that tumor-tissue fluorescence was stronger in the M-HMnO$_2$@ICG group (Figure 6B). Quantification confirmed that fluorescence was significantly more intense in the M-HMnO$_2$@ICG group than in the HMnO$_2$@ICG at different timepoints (Figure 6C). Twenty-four hours after administration, tumor accumulation in the M-HMnO$_2$@ICG group was 1.1 times that in the HMnO$_2$@ICG group. The targeting ability of M-HMnO$_2$@ICG is attributable to its HeLa cell membrane encapsulation, which prevented rapid clearance during circulation and enabled preferential accumulation at tumor sites through homologous targeting. To verify these results, we used ICP-OES to measure Mn concentrations in tumor tissues at different timepoints after M-HMnO$_2$@ICG injection. The highest level was measured at 24 hours after injection (Figure 6D).

The MnO$_2$ in the NP structure degrades responsively in the tumor microenvironment to produce Mn^{2+}, which is considered to be a T1 developer for MRI due to its occupation of five unpaired 3d electrons. Thus, a 7.0-T small-animal MRI system was used to evaluate the tumor-targeting and responsive degradation abilities of M-HMnO$_2$@ICG in vitro. Weak MRI signals were observed for M-HMnO$_2$@ICG in a pH 7.4 solution, whereas the concentration-dependent enhancement of MRI signals was observed for M-HMnO$_2$@ICG in a pH 6.0 solution containing GSH or H$_2$O$_2$ (Figure 6E), confirming the NPs' responsive degradation in the tumor microenvironment. Longitudinal relaxivity coefficients for M-HMnO$_2$@ICG in solutions at pH 7.4, pH 6.0 containing H$_2$O$_2$ and pH 6.0 containing GSH were 0.26, 0.59, and 1.2 $mM^{-1}\cdot s^{-1}$, respectively (Figure 6F). These results suggest that M-HMnO$_2$@ICG releases Mn^{2+} in response to the tumor microenvironment, which enables tumor diagnosis by MRI. To verify this effect in vivo, MRI signals were recorded at 0, 30, and 60 min after the intratumoral injection of M-HMnO$_2$@ICG. Clear MRI signals were observed at 30 min after injection, and their intensity increased gradually over time (Figure 6G). Subsequently, we evaluated MRI effects at tumor sites in vivo after tail vein injection of M-HMnO$_2$@ICG. No significant difference was

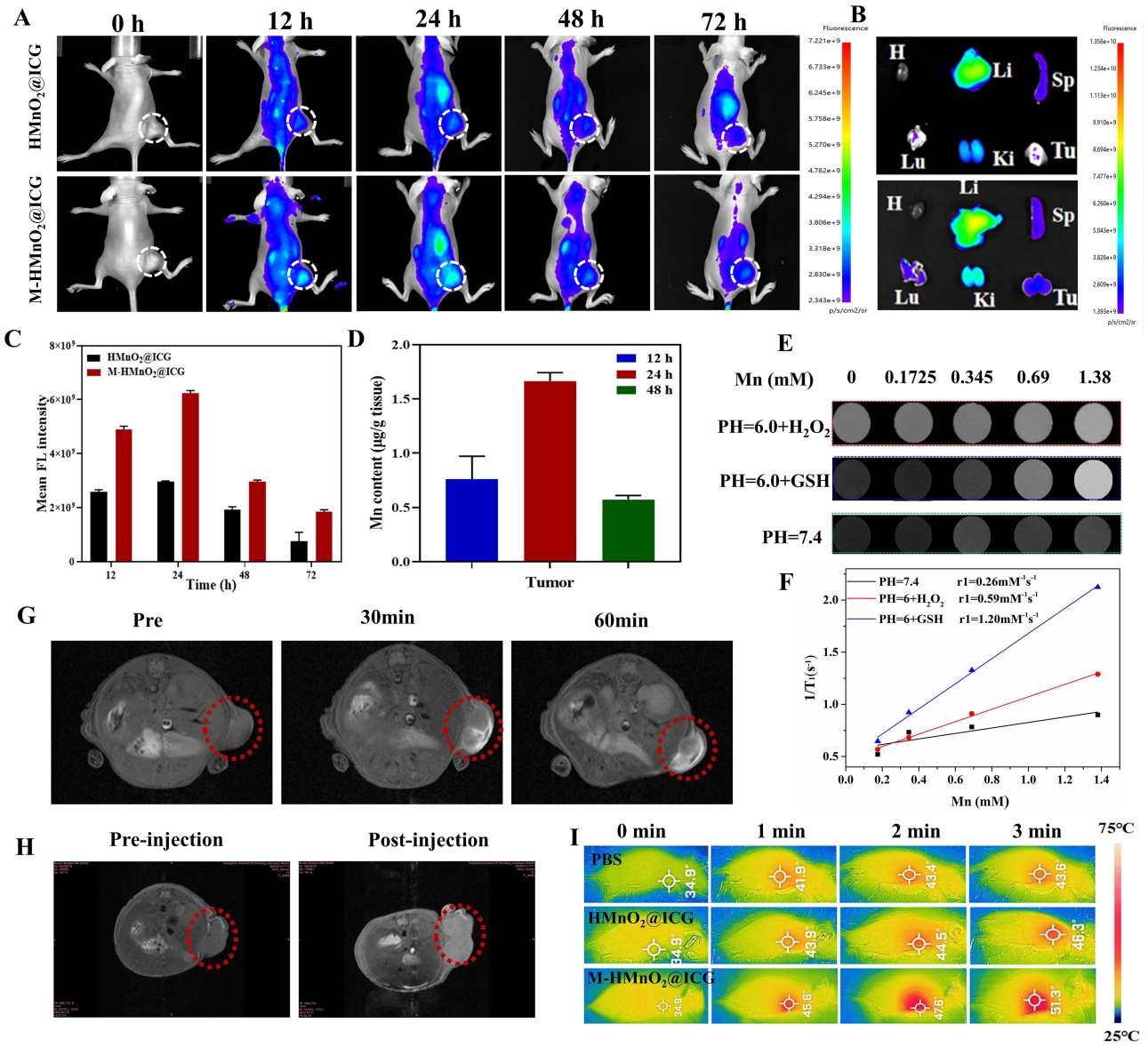

Figure 6 (**A**) In-vivo fluorescence imaging of HeLa tumor–bearing mice at different timepoints after the intravenous injection of $HMnO_2$@ICG and M-$HMnO_2$@ICG, with the subcutaneous tumor area indicated by a white dashed line. (**B**) Ex-vivo imaging of tumors and major organs collected from these mice at 72 h after injection. (**C**) Quantification of fluorescence at tumor sites after injection. (**D**) Mn content in tumor tissues at different timepoints after the intravenous injection of M-$HMnO_2$@ICG. (**E**) T1-weighted MR images of M-$HMnO_2$@ICG dissolved under different pH and redox conditions. (**F**) Longitudinal T1 relaxation rates versus Mn^{2+} concentrations under different conditions. (**G**) In-vivo MR images of HeLa tumor-bearing mice at different timepoints after the intratumoral injection of M-$HMnO_2$@ICG, with the subcutaneous tumor area indicated by a red dashed line. (**H**) In-vivo T1-weighted MR images were obtained 24 h after the tail vein injection of M-$HMnO_2$@ICG, with the subcutaneous tumor area indicated by a red dashed line. (**I**) Photothermograms of HeLa tumor-bearing mice in different treatment groups under laser irradiation (808 nm, 1.35 W/cm^2).

observed between the tumor tissues before M-$HMnO_2$@ICG injection and other tissues. The T1-weighted MRI signals of the tumor tissues were significantly enhanced at 24 h after injection (Figure 6H), further indicating that NPs effectively accumulated and released Mn^{2+} at the tumor sites. Taking advantage of the photothermal conversion ability of M-$HMnO_2$@ICG, we also monitored the NPs' tumor-targeting enrichment and photothermal properties in vivo using NIR thermography. PBS, $HMnO_2$@ICG, and M-$HMnO_2$@ICG were injected via the tail vein into tumor-bearing mice, and laser irradiation (808 nm, 1.35 W/cm^2) was performed for 3 min 24 h later. Compared with PBS (control), M-$HMnO_2$@ICG and $HMnO_2$@ICG significantly increased the tumor tissue temperature, indicating that the NPs had good photothermal conversion abilities in vivo. The photothermal conversion effect of M-$HMnO_2$@ICG was stronger than that of $HMnO_2$@ICG (51.3°C vs 46.3°C, Figure 6I) due to the former's stronger tumor-targeting ability.

In-Vivo Antitumor Treatment and Biosafety

The antitumor effects of M-HMnO$_2$@ICG were evaluated in vivo. When the subcutaneous graft tumor volume had reached 100 mm^3, the tumor-bearing mice were divided randomly into six groups (PBS, NIR, ICG + NIR, HMnO$_2$@ICG, HMnO$_2$@ICG + NIR, and M-HMnO$_2$@ICG + NIR). The treatments were administered by tail vein injection on days 0 and 5, and 3 min laser irradiation of the tumor regions was performed at 24 h after injection (Figure 7A). The body weights of the mice and the tumor volumes were monitored at 2-day intervals for 14 days after the first injection. The body weights of the mice did not change significantly over time in any group, indicating that no treatment had an acute toxic effect (Figure 7B). The tumor volumes increased rapidly over the 14 days in the control and NIR groups (Figure 7C), indicating that cervical cancer is extremely proliferative and that laser irradiation alone has no therapeutic

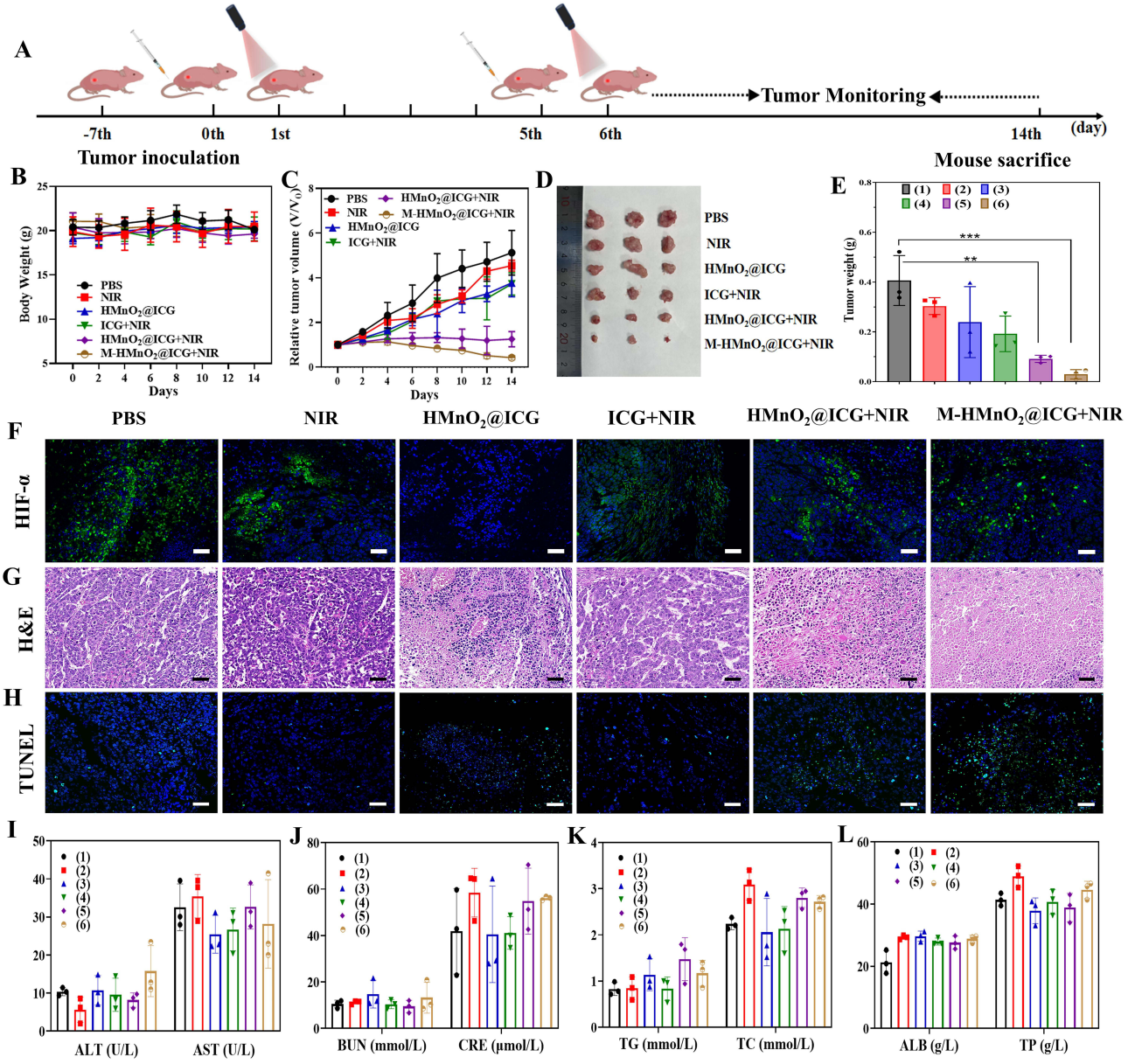

Figure 7 (**A**) Schematic diagram of the treatment of tumor-bearing mice. Mouse body weights (**B**) and relative tumor volumes (**C**). (**D**) Photographs of tumors collected from the mice on day 14 after intravenous injection. (**E**) Tumor tissue weights. Data are expressed as mean ± SD (n = 3). **P < 0.01, ***P < 0.001. (**F**–**H**) H&E, and TUNEL staining and immunofluorescence images of HIF-1α (green; blue, nuclei) in tumor tissues collected after treatment (scale bar: 50 μm). (**I**–**L**) Post-treatment alanine aminotransferase (ALT), aspartate aminotransferase (AST), blood urea nitrogen (BUN), creatinine (CRE), total cholesterol (TC), triglyceride (TG), albumin (ALB), and total protein (TP) levels in HeLa tumor-bearing mice. (1) PBS group, (2) NIR group, (3) HMnO$_2$@ICG group, (4) ICG + NIR group, (5) HMnO$_2$@ICG + NIR group, (6) M-HMnO$_2$@ICG + NIR group. Error bars represent results from three measurements.

https://doi.org/10.2147/IJN.S466042 DovePress

effect on it. The therapeutic effect was limited in the $HMnO_2$@ICG-alone group, indicating that CDT alone is not effective. Similarly, poor tumor inhibition was observed in the ICG + NIR group, indicating that PTT and PDT via ICG alone is not sufficient to inhibit tumor growth under hypoxic conditions. A significant tumor inhibitory effect was observed in the M-$HMnO_2$@ICG + NIR group relative to the other groups, due to homologous targeting to enhance tumor accumulation and PDT/CDT/PTT synergism. The mice were executed after treatment, and the tumor tissues were collected for photography (Figure 7D) and weighing (Figure 7E). The results were consistent with the in-vivo observations, indicating that M-$HMnO_2$@ICG + NIR had the strongest therapeutic effect.

To further validate the synergistic strategy for PDT enhancement, we examined in-vivo hypoxia levels via immunofluorescence staining of mouse tumor tissue sections for HIF-1α. Due to hypoxia in the tumor microenvironment, the PBS and NIR groups showed strong green fluorescence. Green fluorescence (and thus HIF-1α expression) was significantly reduced in the $HMnO_2$@ICG group, suggesting that these NPs could enhance PDT. Fluorescence was also reduced in the M-$HMnO_2$@ICG + NIR group relative to the control group (Figure 7F), attributable to the enhancement of PDT by self-oxygenation and CDT by the warming effect of photothermal conversion. H&E staining of the tumor tissues revealed the apoptosis of almost all tumor cells in the M-$HMnO_2$@ICG + NIR group (Figure 7G). TUNEL analysis showed certain degrees of apoptosis in the ICG, $HMnO_2$@ICG, and $HMnO_2$@ICG + NIR groups relative to the control and NIR groups, with the strongest apoptosis-indicating fluorescence observed in the M-$HMnO_2$@ICG + NIR group (Figure 7H). Based on these findings, as well as preferential accumulation at tumor sites and effective, homologous, and passive tumor targeting due to NP encapsulation, M-$HMnO_2$@ICG + NIR contributed to the synergistic antitumor effect of CDT/PTT/PDT.

Serum biochemical indexes did not change in any treatment group (Figure 7I–L), indicating that the treatments had excellent biosafety. H&E staining of major organs revealed no significant morphological change or inflammatory infiltration (Figure S13), confirming the long-term biosafety of the nanomaterials. The in-vivo antitumor treatment effects were consistent with the in-vitro results.

Conclusion

In this study, we used hollow mesoporous MnO_2 as a carrier to construct a simple, economical, green, and convenient nanoplatform for efficient ICG loading. We demonstrated that the MnO_2 degraded responsively in the tumor microenvironment to effectively release aggregated ICG, consume intracellular GSH in tumor cells, and produce Fenton-like effects while catalyzing O_2 production in tumor cells for sensitization to ICG-mediated PDT under laser irradiation. In addition, the good photothermal properties of ICG contributed to the enhancement of ROS-generating antitumor strategies. The $HMnO_2$@ICG NPs homologously targeted tumor cells and immune escape due to their HeLa cell membrane surface coatings. We systematically validated the good antitumor effects of M-$HMnO_2$@ICG at the in-vivo and in-vitro levels. We designed the nanoplatform to enable turn-on with MRI and accurate guidance with fluorescence and photothermal imaging. Thus, the M-$HMnO_2$@ICG NPs offer a new strategy for the active targeting of cervical cancer via synergistically enhancing PTT/PDT/CDT and the use of the tumor cell membrane camouflage. As multi-modal imaging-guided tumor microenvironment–responsive nanoplatforms, they provide new hope for the effectiveness of ROS-related treatment modalities.

Acknowledgments

This work was supported by grants-in-aid for scientific research from the National Natural Science Foundation of China (number U20A20339), the National Natural Science Foundation of China (number 82271880).

Disclosure

The authors report no conflicts of interest in this work.

References

1. Sung H, Ferlay J, Siegel RL, et al. Global Cancer Statistics 2020: GLOBOCAN estimates of incidence and mortality worldwide for 36 cancers in 185 countries. *CA*. 2021;71(3):209–249. doi:10.3322/caac.21660
2. Abu-Rustum NR, Yashar CM, Arend R, et al. NCCN Guidelines® insights: cervical cancer, version 1.2024. *J National Compr Cancer Network*. 2023;21(12):1224–1233. doi:10.6004/jnccn.2023.0062
3. Iwata T, Machida H, Matsuo K, et al. The validity of the subsequent pregnancy index score for fertility-sparing trachelectomy in early-stage cervical cancer. *Fertil Sterility*. 2021;115(5):1250–1258. doi:10.1016/j.fertnstert.2020.09.162
4. Slama J, Runnebaum IB, Scambia G, et al. Analysis of risk factors for recurrence in cervical cancer patients after fertility-sparing treatment: the FERTIlity Sparing Surgery retrospective multicenter study. *Am J Clin Exp Obstet Gynecol*. 2023;228(4):443.e441–443.e410. doi:10.1016/j.ajog.2022.11.1295
5. Zeien J, Qiu W, Triay M, et al. Clinical implications of chemotherapeutic agent organ toxicity on perioperative care. *Biomed Pharmacother*. 2022;146:112503. doi:10.1016/j.biopha.2021.112503
6. Wang X, Liu S, Guan Y, Ding J, Ma C, Xie Z. Vaginal drug delivery approaches for localized management of cervical cancer. *Adv Drug Delivery Rev*. 2021;174:114–126. doi:10.1016/j.addr.2021.04.009
7. Luo L, Zhou H, Wang S, et al. The application of nanoparticle-based imaging and phototherapy for female reproductive organs diseases. *Small*. 2023:e2207694. doi:10.1002/smll.202207694
8. He P, Yang G, Zhu D, et al. Biomolecule-mimetic nanomaterials for photothermal and photodynamic therapy of cancers: bridging nanobiotechnology and biomedicine. *J Nanobiotechnology*. 2022;20(1):483. doi:10.1186/s12951-022-01691-4
9. Li X, Lovell JF, Yoon J, Chen X. Clinical development and potential of photothermal and photodynamic therapies for cancer. *Nat Rev Clin Oncol*. 2020;17(11):657–674. doi:10.1038/s41571-020-0410-2
10. Jung HS, Verwilst P, Sharma A, Shin J, Sessler JL, Kim JS. Organic molecule-based photothermal agents: an expanding photothermal therapy universe. *Chem Soc Rev*. 2018;47(7):2280–2297. doi:10.1039/c7cs00522a
11. Seung Lee J, Kim J, Y-s Y, T-i K. Materials and device design for advanced phototherapy systems. *Adv Drug Delivery Rev*. 2022;186. doi:10.1016/j.addr.2022.114339
12. Li S, Meng X, Peng B, et al. Cell membrane-based biomimetic technology for cancer phototherapy: mechanisms, recent advances and perspectives. *Acta Biomater*. 2024;174:26–48. doi:10.1016/j.actbio.2023.11.029
13. Zhong YT, Cen Y, Xu L, Li SY, Cheng H. Recent progress in carrier-free nanomedicine for tumor phototherapy. *Adv Healthc Mater*. 2023;12(4):e2202307. doi:10.1002/adhm.202202307
14. Liu Y, Bhattarai P, Dai Z, Chen X. Photothermal therapy and photoacoustic imaging via nanotheranostics in fighting cancer. *Chem Soc Rev*. 2019;48(7):2053–2108. doi:10.1039/c8cs00618k
15. Nasseri B, Turk M, Kosemehmetoglu K, et al. The pimpled gold nanosphere: a superior candidate for plasmonic photothermal therapy. *Int J Nanomed*. 2020;15:2903–2920. doi:10.2147/ijn.S248327
16. Meng Z, Xue H, Wang T, et al. Aggregation-induced emission photosensitizer-based photodynamic therapy in cancer: from chemical to clinical. *J Nanobiotechnology*. 2022;20(1):344. doi:10.1186/s12951-022-01553-z
17. Xu X, Huang B, Zeng Z, et al. Broaden sources and reduce expenditure: tumor-specific transformable oxidative stress nanoamplifier enabling economized photodynamic therapy for reinforced oxidation therapy. *Theranostics*. 2020;10(23):10513–10530. doi:10.7150/thno.49731
18. Wang R, Li X, Yoon J. Organelle-targeted photosensitizers for precision photodynamic therapy. *ACS Appl Mater Interfaces*. 2021;13(17):19543–19571. doi:10.1021/acsami.1c02019
19. Overchuk M, Weersink RA, Wilson BC, Zheng G. Photodynamic and photothermal therapies: synergy opportunities for nanomedicine. *ACS Nano*. 2023;17(9):7979–8003. doi:10.1021/acsnano.3c00891
20. Wang Y, Luo S, Wu Y, et al. Highly penetrable and on-demand oxygen release with tumor activity composite nanosystem for photothermal/photodynamic synergetic therapy. *ACS Nano*. 2020;14(12):17046–17062. doi:10.1021/acsnano.0c06415
21. Kong C, Chen X. Combined photodynamic and photothermal therapy and immunotherapy for cancer treatment: a review. *Int j Nanomed*. 2022;17:6427–6446. doi:10.2147/ijn.S388996
22. Agostinis P, Berg K, Cengel KA, et al. Photodynamic therapy of cancer: an update. *CA*. 2011;61(4):250–281. doi:10.3322/caac.20114
23. Cao W, Zhu Y, Wu F, et al. Three birds with one stone: acceptor engineering of hemicyanine dye with NIR-II emission for synergistic photodynamic and photothermal anticancer therapy. *Small*. 2022;18(49):e2204851. doi:10.1002/smll.202204851
24. Wu P, Zhu Y, Chen L, Tian Y, Xiong H. A fast-responsive OFF–ON Near-infrared-II fluorescent probe for in vivo detection of hypochlorous acid in rheumatoid arthritis. *Anal Chem*. 2021;93(38):13014–13021. doi:10.1021/acs.analchem.1c02831
25. Wu P, Zhu Y, Liu S, Xiong H. Modular design of high-brightness ph-activatable near-infrared bodipy probes for noninvasive fluorescence detection of deep-seated early breast cancer bone metastasis: remarkable axial substituent effect on performance. *ACS Cent Sci*. 2021;7(12):2039–2048. doi:10.1021/acscentsci.1c01066
26. Porcu EP, Salis A, Gavini E, Rassu G, Maestri M, Giunchedi P. Indocyanine green delivery systems for tumour detection and treatments. *Biotechnol Adv*. 2016;34(5):768–789. doi:10.1016/j.biotechadv.2016.04.001
27. Sun X, He G, Xiong C, et al. One-pot fabrication of hollow porphyrinic mof nanoparticles with ultrahigh drug loading toward controlled delivery and synergistic cancer therapy. *ACS Appl Mater Interfaces*. 2021;13(3):3679–3693. doi:10.1021/acsami.0c20617
28. Jaiswal S, Roy R, Dutta SB, et al. Role of doxorubicin on the loading efficiency of ICG within silk fibroin nanoparticles. *ACS Biomater Sci Eng*. 2022;8(7):3054–3065. doi:10.1021/acsbiomaterials.1c01616
29. Chaudhary Z, Khan GM, Abeer MM, et al. Efficient photoacoustic imaging using indocyanine green (ICG) loaded functionalized mesoporous silica nanoparticles. *Biomater Sci*. 2019;7(12):5002–5015. doi:10.1039/c9bm00822e
30. Ma Y, Chen L, Li X, et al. Rationally integrating peptide-induced targeting and multimodal therapies in a dual-shell theranostic platform for orthotopic metastatic spinal tumors. *Biomaterials*. 2021:275. doi:10.1016/j.biomaterials.2021.120917
31. Sun Y, Wang Y, Liu Y, et al. Intelligent tumor microenvironment-activated multifunctional nanoplatform coupled with turn-on and always-on fluorescence probes for imaging-guided cancer treatment. *ACS Appl Mater Interfaces*. 2021;13(45):53646–53658. doi:10.1021/acsami.1c17642

32. Fang C, Yan P, Ren Z, et al. Multifunctional MoO2-ICG nanoplatform for 808nm-mediated synergetic photodynamic/photothermal therapy. *Appl. Mater. Today*. 2019;15:472–481. doi:10.1016/j.apmt.2019.03.008
33. Deng K, Hou Z, Deng X, Yang P, Li C, and Lin J. Enhanced antitumor efficacy by 808 nm laser-induced synergistic photothermal and photodynamic therapy based on a indocyanine-green-attached W18O49 nanostructure. *Adv Funct Mater*. 2015;25(47):7280–7290. doi:10.1002/adfm.201503046
34. Xue P, Yang R, Sun L, et al. Indocyanine green-conjugated magnetic prussian blue nanoparticles for synchronous photothermal/photodynamic tumor therapy. *Nano-Micro Lett*. 2018;10(4):74. doi:10.1007/s40820-018-0227-z
35. Fukasawa T, Hashimoto M, Nagamine S, et al. Fabrication of ICG dye-containing particles by growth of polymer/salt aggregates and measurement of photoacoustic signals. *Chem Lett*. 2014;43(4):495–497. doi:10.1246/cl.131088
36. Yu J, Javier D, Yaseen MA, et al. Self-assembly synthesis, tumor cell targeting, and photothermal capabilities of antibody-coated indocyanine green nanocapsules. *J Am Chem Soc*. 2010;132(6):1929–1938. doi:10.1021/ja908139y
37. Sun Q, Wang Z, Liu B, et al. Self-generation of oxygen and simultaneously enhancing photodynamic therapy and MRI effect: an intelligent nanoplatform to conquer tumor hypoxia for enhanced phototherapy. *Chem Eng J*. 2020:390. doi:10.1016/j.cej.2020.124624
38. Huang P-Y, Zhu -Y-Y, Zhong H, et al. Autophagy-inhibiting biomimetic nanodrugs enhance photothermal therapy and boost antitumor immunity. *Biomater Sci*. 2022;10(5):1267–1280. doi:10.1039/d1bm01888d
39. Chen X, Zhao C, Liu D, et al. Intelligent Pd1.7Bi@CeO2 nanosystem with dual-enzyme-mimetic activities for cancer hypoxia relief and synergistic photothermal/photodynamic/chemodynamic therapy. *ACS Appl Mater Interfaces*. 2023;15(18):21804–21818. doi:10.1021/acsami.3c00056
40. Cheng Y, Wen C, Sun YQ, Yu H, Yin XB. Mixed-Metal MOF-derived hollow porous nanocomposite for trimodality imaging guided reactive oxygen species-augmented synergistic therapy. *Adv Funct Mater*. 2021;31(37):2. doi:10.1002/adfm.202104378.
41. Yu J, Yaseen MA, Anvari B, Wong MS. Synthesis of near-infrared-absorbing nanoparticle-assembled capsules. *Chem Mater*. 2007;19(6):1277–1284. doi:10.1021/cm062080x
42. Zeng W, Zhang H, Deng Y, et al. Dual-response oxygen-generating MnO2 nanoparticles with polydopamine modification for combined photothermal-photodynamic therapy. *Chem Eng J*. 2020:389. doi:10.1016/j.cej.2020.124494
43. Liu X, Li R, Zhou Y, et al. An all-in-one nanoplatform with near-infrared light promoted on-demand oxygen release and deep intratumoral penetration for synergistic photothermal/photodynamic therapy. *J Colloid Interface Sci*. 2022;608:1543–1552. doi:10.1016/j.jcis.2021.10.082
44. Gao J, Qin H, Wang F, et al. Hyperthermia-triggered biomimetic bubble nanomachines. *Nat Commun*. 2023;14(1):4867. doi:10.1038/s41467-023-40474-9
45. Xi Y, Xie X, Peng Y, Liu P, Ding J, Zhou W. DNAzyme-adsorbed polydopamine@MnO2 core–shell nanocomposites for enhanced photothermal therapy via the self-activated suppression of heat shock protein 70. *Nanoscale*. 2021;13(9):5125–5135. doi:10.1039/d0nr08845e
46. Sun W, Xu Y, Yao Y, et al. Self-oxygenation mesoporous MnO2 nanoparticles with ultra-high drug loading capacity for targeted arteriosclerosis therapy. *J Nanobiotechnology*. 2022;20(1):88. doi:10.1186/s12951-022-01296-x
47. Gostynski R, Conradie J, Erasmus E. Significance of the electron-density of molecular fragments on the properties of manganese(iii) β-diketonato complexes: an XPS and DFT study. *RSC Adv*. 2017;7(44):27718–27728. doi:10.1039/c7ra04921h
48. Quan B, S-H Y, Chung DY, et al. Single source precursor-based solvothermal synthesis of heteroatom-doped graphene and its energy storage and conversion applications. *Sci Rep*. 2014;4:5639. doi:10.1038/srep05639
49. Liu J, Li RS, Zhang L, et al. Enzyme-activatable polypeptide for plasma membrane disruption and antitumor immunity elicitation. *Small*. 2023;19(24):e2206912. doi:10.1002/smll.202206912
50. Xu B, Zeng F, Deng J, et al. A homologous and molecular dual-targeted biomimetic nanocarrier for EGFR-related non-small cell lung cancer therapy. *Bioact Mater*. 2023;27:337–347. doi:10.1016/j.bioactmat.2023.04.005
51. Fan Y, Cui Y, Hao W, et al. Carrier-free highly drug-loaded biomimetic nanosuspensions encapsulated by cancer cell membrane based on homology and active targeting for the treatment of glioma. *Bioact Mater*. 2021;6(12):4402–4414. doi:10.1016/j.bioactmat.2021.04.027
52. Du X, Zhang Y, Zhang Y, et al. Cancer cell membrane camouflaged biomimetic nanosheets for enhanced chemo-photothermal-starvation therapy and tumor microenvironment remodeling. *Appl Mater Today*. 2022;29. doi:10.1016/j.apmt.2022.101677
53. Guan S, Liu X, Li C, et al. Intracellular mutual amplification of oxidative stress and inhibition multidrug resistance for enhanced sonodynamic/chemodynamic/chemo therapy. *Small*. 2022;18(13):e2107160. doi:10.1002/smll.202107160